

RI-(S)MOM to $\overline{\text{MS}}$ conversion for B_K at two-loop order

Martin Gorbahn,^a Sebastian Jäger^b and Sandra Kvedaraitė^c

^a*Department of Mathematical Sciences, University of Liverpool, Liverpool, L69 7ZL, UK*

^b*Department of Physics and Astronomy, University of Sussex, Falmer, Brighton BN1 9QH, United Kingdom*

^c*Departamento de Física Teórica y del Cosmos, Universidad de Granada, Campus de Fuentenueva, E-18071 Granada, Spain*

E-mail: Martin.Gorbahn@liverpool.ac.uk, S.Jaeger@sussex.ac.uk, skvedaraitė@ugr.es

ABSTRACT:

The Kaon bag parameter \hat{B}_K plays a critical role in constraining the parameters of the CKM matrix and in probing physics beyond the Standard Model. In this work, we improve the precision of \hat{B}_K to next-to-next-to-leading order (NNLO) and provide world averages for both 3- and 4-flavour theories. In the course of this, as our main technical development, we carry out the two-loop matching between the RI-(S)MOM and $\overline{\text{MS}}$ schemes. Our world averages combine all available lattice data, including conversion between the 3- and 4-flavour theories as appropriate. We obtain the result $\hat{B}_K^{(f=3)} = 0.7627(60)$, which comprises the complete set of 3- and 4-flavour lattice results and can be used directly in phenomenological applications. The error is dominated by lattice uncertainties and missing higher-order corrections (residual scale dependence). Our averages include a PDG rescaling factor of 1.28 reflecting a mild tension among the lattice inputs after inclusion of NNLO corrections in the scheme conversion and matching across flavour thresholds. Our averages imply an updated value $|\epsilon_K| = 2.171(65)_{\text{pert.}}(71)_{\text{non-pert.}}(153)_{\text{param.}} \times 10^{-3}$. We briefly discuss applications of our results to D -meson mixing.

Contents

1	Introduction	2
2	Operator renormalization and matching between schemes	3
2.1	Momentum subtraction schemes	3
2.2	$\overline{\text{MS}}$ NDR scheme	5
3	Matching calculation	6
3.1	Tree-level amplitude	6
3.2	Bilinears and invariants	7
3.3	Matrix elements entering the total amplitude	8
3.4	Projectors and evanescent structures	8
3.5	Obtaining coefficients A_i and \tilde{A}_i	9
3.6	Obtaining the (S)MOM projections	10
4	Loop calculation	11
4.1	Amplitude at NLO	11
4.2	Amplitude at NNLO	12
4.3	Defining two-loop topologies	12
4.4	Master integrals and evaluation	14
4.5	Operators in Brod–Gorbahn basis	15
4.6	Renormalized amplitude	16
5	Results	16
5.1	$C_{B_K}^{(\text{S})\text{MOM} \rightarrow \overline{\text{MS}}}$ up to NNLO	17
5.2	Conversion to the RGI bag factor	18
5.3	$B_K^{\overline{\text{MS}}}$, \hat{B}_K and their residual scale dependence	19
5.4	Matching between number of flavours	22
5.5	\hat{B}_K global average	24
5.6	ϵ_K updated value	25
5.7	D meson mixing	25
6	Conclusions	26
A	Fierz-evanescent operators	26
B	$\overline{\text{MS}}$ renormalization constants	27
C	Operator anomalous dimensions	28
D	One-loop counterterms	28

1 Introduction

The Kaon bag parameter \hat{B}_K [1] is one of the key quantities in helping us understand the neutral Kaon mixing as it enters a dominant contribution to indirect CP violation in the Kaon system ϵ_K . Precise determination of \hat{B}_K allows us to constrain the CKM matrix and probe for physics beyond the Standard Model, with [2–5]

$$|\epsilon_K| = \kappa_\epsilon C_\epsilon \hat{B}_K |V_{cb}|^2 \lambda^2 \bar{\eta} \times (|V_{cb}|^2 (1 - \bar{\rho}) \eta_{tt} S_{tt}(x_t) - \eta_{ut} S_{ut}(x_c, x_t)). \quad (1.1)$$

Here $S_{tt}(x_t)$ and $S_{uu}(x_t)$, with $x_t = m_t^2/m_W^2$, are the leading-order weak-scale short distance contributions, due to the diagrams in Figure 1, and η_{tt} and η_{ut} comprise perturbative QCD and QED corrections to them [6–10], including integrating out the bottom and charm quark and physics at scales between, and together give a scale- and scheme-independent combination. $\kappa_\epsilon = 0.94(2)(1 + \delta_{m_c})$ are subdominant corrections [4] not included in \hat{B}_K , where $\delta_{m_c} = 0.010(3)$ incorporates an extended analysis of power corrections [11]. V_{cb} , $\bar{\rho}$ and $\bar{\eta}$ represent CKM input. The remaining parametric input is collected in $C_\epsilon = (G_F^2 F_K^2 M_K M_W^2)/(6\sqrt{2}\pi^2 \Delta M_K)$. Experimentally, ϵ_K has been precisely measured as $|\epsilon_K|_{\text{exp}} = (2.228 \pm 0.011) \times 10^{-3}$ [12]. As for the theory prediction, the perturbative, non-perturbative and parametric uncertainties were found to be at around 3%, 3.5% and 7% respectively [2].

The remaining ingredient, the renormalization-scale and scheme-independent bag factor is a nonperturbative object and can be defined as

$$\hat{B}_K^{(f=3)} = \lim_{\mu \rightarrow \infty} B_K^A(\mu) \alpha_s(\mu)^{-2/9}, \quad (1.2)$$

where

$$B_K^A(\mu) = \frac{\langle \bar{K}^0 | Q^A(\mu) | K^0 \rangle}{\frac{8}{3} F_K^2 M_K^2}. \quad (1.3)$$

Here F_K the Kaon decay constant, M_K the Kaon mass, and $Q^A(\mu)$ is the unique dimension-six $\Delta S = \Delta D = 2$ operator,

$$Q = (\bar{s}_L^\alpha \gamma_\mu d_L^\alpha) (\bar{s}_L^\beta \gamma^\mu d_L^\beta), \quad (1.4)$$

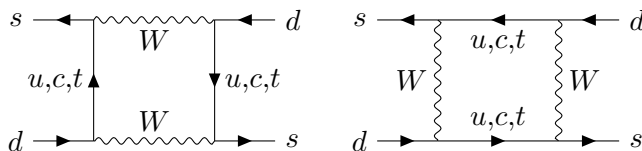


Figure 1. Leading contributions to $K^0 - \bar{K}^0$ mixing

renormalized in an arbitrary scheme A . To any given order in perturbation theory, one has

$$\hat{B}_K = C^{A \rightarrow \text{RGI}}(\mu) B_K^A(\mu),$$

with $C^{A \rightarrow \text{RGI}} = 1 + \mathcal{O}(\alpha_s)$. One can also write a formula for ϵ_K which avoids the perturbative treatment of the charm scale, which then involves additional nonlocal nonperturbative contributions together with a four-flavour version of \hat{B}_K .

The current status of \hat{B}_K is summarized by the average of $\hat{B}_K = 0.7533(91)$ [13], based on a variety of Lattice calculations with 2+1 active flavors. These calculations use different intermediate schemes for the evaluation of the matrix elements, which have to be transformed to the renormalization-group-invariant (RGI) bag parameter.

The objective of the present paper is to provide a result for \hat{B}_K to NNLO accuracy comprising all available $f = 3$ and $f = 4$ lattice calculations of B_K . To this end, we compute the two-loop conversion factor $C^{(\text{S})\text{MOM} \rightarrow \overline{\text{MS}}}$ between the RI-(S)MOM momentum-space renormalization schemes [14, 15], which can be implemented on the lattice, and the $\overline{\text{MS}}$ scheme. These conversion factors can then be combined with existing computations for the matching across the charm threshold [7] and for the conversion from the $\overline{\text{MS}}$ scheme to RGI, to provide the desired result. We will present the average both in the form of a 3-flavour version $\hat{B}_K^{(f=3)}$, which can be directly used in equation (1.1), and a 4-flavour version $\hat{B}_K^{(f=4)}$ which may be useful for future phenomenological applications where the charm quark is treated nonperturbatively. We stress that each result comprises all 3- and 4-flavour lattice inputs.

The remainder of this work is organized as follows. In Section 2 we review the momentum-space subtraction and $\overline{\text{MS}}$ schemes for operator renormalization. In Sections 3 and 4 we describe the calculation of the amplitude of a amputated four-point Green's function, first focusing on the overall set-up of the matching calculation, followed by a detailed discussion of the loop calculation and renormalization of the amplitude. Finally, in Section 5 we present our results, including the NNLO conversion factors, their residual scale dependence, world averages for \hat{B}_K , and an updated prediction for ϵ_K value. We also provide an RGI-invariant parameter for D-meson mixing.

2 Operator renormalization and matching between schemes

In this section we review the renormalization of four-quark operators in $\overline{\text{MS}}$ NDR and momentum subtraction schemes. We also discuss the matching between the two schemes. For a comprehensive introduction to the treatment of four-quark operators we refer to [5, 16] and references therein.

2.1 Momentum subtraction schemes

The RI schemes are defined by imposing renormalization conditions on projected two-point and four-point functions for certain off-shell kinematics. Several variants of the RI scheme exist in the literature, that differ by the kinematics for the renormalization condition of the four-point functions and the choice of projectors used for the two-point and four-point

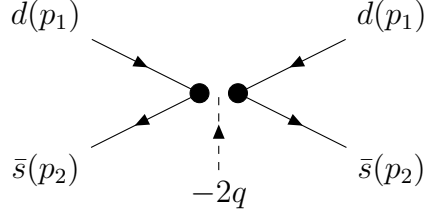


Figure 2. The SMOM momentum subtraction point for a four-quark operator is defined by $p_1^2 = p_2^2 = q^2 = -\mu^2$, while the MOM momentum subtraction point fulfils $p_1^2 = p_2^2 = -\mu^2$ and $q^2 = 0$. The solid black lines with arrows indicate fermion and momentum flow, the dashed line with arrow indicates momentum flow into the vertex.

functions. Two different projectors are used for the two point function, and we will denote the projector associated with a given RI scheme by $s(\text{RI}) = \not{q}$ and $s(\text{RI}) = \gamma$ in the following. To fix our notation, we write for the connected fermion two-point function S

$$(2\pi)^4 i S(p)_{\alpha\beta} \delta^4(p-q) \delta^{ij} = \int d^4x d^4y e^{i(p\cdot x - q\cdot y)} \langle 0 | T \{ \psi_\alpha^i(x) \bar{\psi}_\beta^j(y) \} | 0 \rangle, \quad (2.1)$$

and define the projected scalar amplitudes of the renormalized two-point function S^A as

$$\sigma^{(A, \not{q})} \equiv \frac{1}{4 p^2} \text{Tr} [(S^A)^{-1}(p) \not{p}], \quad (2.2)$$

and

$$\sigma^{(A, \gamma)} \equiv \frac{1}{16} \text{Tr} \left[\gamma^\mu \frac{\partial (S^A)^{-1}(p)}{\partial p^\mu} \right]. \quad (2.3)$$

The renormalization condition for an RI scheme A with $s(A) = \gamma$ or $s(A) = \not{q}$ is then given by $\sigma^{(A, \gamma)} = 1$ and $\sigma^{(A, \not{q})} = 1$ respectively. The kinematics is always fixed to $p^2 = -\mu^2$ at the renormalization point. Writing for the amputated four-point function $\Lambda_{\rho\sigma\tau\nu}^{ijkl}$ with an operator insertion O

$$\begin{aligned} & \int d^4x d^4x_{1,2,3,4} e^{-i(2q\cdot x + p_1\cdot x_1 - p_2\cdot x_2 + p_1\cdot x_3 - p_2\cdot x_4)} \langle 0 | T \{ \bar{d}_\beta^j(x_1) s_\alpha^i(x_2) \bar{d}_\delta^l(x_3) s_\gamma^k(x_4) O(x) \} | 0 \rangle \\ &= (2\pi)^4 S(p_1)_{\alpha\rho} S(p_2)_{\beta\sigma} S(p_3)_{\gamma\tau} S(p_4)_{\delta\nu} \Lambda_{\rho\sigma\tau\nu}^{ijkl}(O) \delta^4(2q - 2(p_1 - p_2)), \end{aligned} \quad (2.4)$$

we define the scalar functions

$$\lambda^{(A, \text{RI})} \equiv \Lambda_{\alpha\beta\gamma\delta}^{A,ijkl} \mathcal{P}_{\text{RI}\alpha\beta, \gamma\delta}^{ijkl}, \quad (2.5)$$

for RI schemes at suitable kinematics with projectors P_{RI} that satisfy $\Lambda_{\alpha\beta\gamma\delta}^{(\text{tree}),ijkl} \mathcal{P}_{\text{RI}\alpha\beta, \gamma\delta}^{ijkl} = 1$.

Two different kinematics are considered for this scalar four-point function in the RI schemes in the literature:

- MOM, where $p_1^2 = p_2^2 = -\mu^2$ and $q^2 \equiv (p_1 - p_2)^2 = 0$, and

- SMOM, where $p_1^2 = p_2^2 = q^2 = -\mu^2$.

The two projection operators used for SMOM are

$$P_{(\gamma\mu),\alpha\beta,\gamma\delta}^{ij,kl} = \frac{(\gamma^\nu)_{\beta\alpha}(\gamma\nu)_{\delta\gamma} + (\gamma^\nu\gamma^5)_{\beta\alpha}(\gamma\nu\gamma^5)_{\delta\gamma}}{256N_c(N_c + 1)} \delta_{ij}\delta_{kl}, \quad \text{RI-(S)MOM}, \quad (2.6)$$

$$P_{(\not{q}),\alpha\beta,\gamma\delta}^{ij,kl} = \frac{(\not{q})_{\beta\alpha}(\not{q})_{\delta\gamma} + (\not{q}\gamma^5)_{\beta\alpha}(\not{q}\gamma^5)_{\delta\gamma}}{64q^2N_c(N_c + 1)} \delta_{ij}\delta_{kl}, \quad \text{RI-SMOM}, \quad (2.7)$$

where N_c is the number of colours, i, j, k, l colour and $\alpha, \beta, \gamma, \delta$ spinor indices [17]. Only $P_{(\gamma\mu),\alpha\beta,\gamma\delta}^{ij,kl}$ is used for MOM kinematics. Having multiple projectors and momentum subtraction configurations allows us to assess the systematic uncertainties resulting from the choice of scheme.

For any two renormalization schemes A and B , the operator Q_{S2} and the quark field ψ are related by a finite conversion factor

$$O^A = \mathcal{C}_O^{A \rightarrow B} O^B, \quad (2.8)$$

which can be computed perturbatively from the scalar-two point function σ and the scalar-four point function λ in a given scheme. The four RI-SMOM conversion factors are

$$\mathcal{C}_O^{A \rightarrow (l,s)} = \lambda^{A,l} (\sigma^{A,s})^2, \quad s, l \in \{\not{q}, \gamma\}, \quad (2.9)$$

where all $\lambda^{A,l}$ are evaluated for SMOM kinematics. For RI-MOM we have

$$\mathcal{C}_O^{A \rightarrow \text{RI-MOM}} = \lambda^{A,\gamma} (\sigma^{A,\not{q}})^2, \quad (2.10)$$

where $\lambda^{A,\gamma}$ is evaluated for MOM kinematics.

2.2 $\overline{\text{MS}}$ NDR scheme

$\overline{\text{MS}}$ schemes, within the context of dimensional regularisation, are constructed explicitly out of the bare operators. In general, the renormalized operators involve several bare operators, which would lead to a renormalization

$$Q_i^{\text{ren}}(\mu) = \sum_j Z_{ij}(\mu) Q_j^{\text{bare}}, \quad (2.11)$$

where $Z_{ij}(\mu)$ is a matrix of renormalization constants. In our case, we have only one physical bare operator Q^B and a single renormalization constant Z_{QQ} . In dimensional regularization there are additional operators E_i^B , as a consequence of the larger Dirac algebra in $D \neq 4$ compared to $D = 4$. They can be chosen such that they vanish at tree-level in $D = 4$ and are known as evanescent operators. For the renormalized four-quark operator Q defined in Eq.(1.4), we have

$$Q^{\text{NDR}} = Z_{QQ} Q^B + \sum_i Z_{QE_i} E_i^B, \quad (2.12)$$

where ‘NDR’ specifies anti-commuting γ^5 and Z_{QQ} and Z_{QE_i} are renormalization constants. The Z -factors are defined such that $g_s(\mu)$ and $\langle Q^{\text{NDR}} \rangle$ (for renormalized quark fields) have

a finite limit $\epsilon \rightarrow 0$. The Z factors are singular as $\epsilon \rightarrow 0$ and, for $\overline{\text{MS}}$, are taken equal to the principal parts of their Laurent expansions (i.e. containing only poles in ϵ).

At loop level, evanescent operators E_i require renormalization just like the physical operators

$$E_i^{\text{NDR}} = Z_{E_i E_j} E_j^B + Z_{E_i Q} Q^B. \quad (2.13)$$

While the $Z_{E_i E_j}$ can again be chosen to be the principal parts of their Laurent series, a finite $Z_{E_i Q}$ is generally required in order to have $\langle E_i^{\text{NDR}} \rangle = 0$ also at loop level. The E_i^{NDR} renormalized in such a fashion are known as evanescent operators, and in particular give vanishing contributions to physical matrix elements.

3 Matching calculation

In this section, we present a method to obtain the RI-(S)MOM projections of the full amplitude up to two-loop order by computing only projections of direct diagrams. The reason for this is that we would like to avoid performing tensor reduction at two-loop order by contracting spinor indices in the beginning. This means, however, that the γ_5 can be treated without ambiguities only for direct diagrams.

The section is organised as follows. In Section 3.1 we examine the structure of $\Lambda_{\alpha\beta,\gamma\delta}^{ij,kl}$ and define direct diagrams. In Section 3.2 we investigate what Lorentz structures are going to appear in the two-loop calculation. Since we are computing only direct diagrams, there are additional Lorentz structures involving external momenta that need to be considered in order to reconstruct the full amplitude. Hence, in Section 3.3 we define further tree-level matrix elements corresponding to the additional structures. We also write down the amplitude in terms of the matrix elements. As we introduce new operators we need a way to disentangle them, therefore, in Section 3.4 we define a new set of projectors. Along with those, we present an extended basis of evanescent operators. In Section 3.5, we then proceed to write down the direct amplitude and explain how we obtain the coefficients in front of the tree-level matrix elements. Finally, in Section 3.6 we discuss how to extract the projections $P_{(1)}$ and $P_{(2)}$ of the full amplitude from these coefficients.

3.1 Tree-level amplitude

Let us start by considering the tree-level matrix element corresponding to the insertion of operator Q at RI-(S)MOM kinematics as

$$\begin{aligned} \langle Q \rangle &\equiv \Lambda_{\alpha\beta\gamma\delta}^{ijkl}(Q) = 2 \left((\gamma^\mu P_L)_{\alpha\beta} (\gamma_\mu P_L)_{\gamma\delta} \delta^{ij} \delta^{kl} - (\gamma^\mu P_L)_{\alpha\delta} (\gamma_\mu P_L)_{\gamma\beta} \delta^{il} \delta^{kj} \right) \\ &\equiv 2 \gamma^\mu P_L \otimes \gamma_\mu P_L \ 1 \otimes 1 - 2 \gamma^\mu P_L \tilde{\otimes} \gamma_\mu P_L \ 1 \tilde{\otimes} 1 \\ &\equiv 2 Q^s \ 1 \otimes 1 - 2 \tilde{Q}^s \ 1 \tilde{\otimes} 1, \end{aligned} \quad (3.1)$$

where we use the superscript ‘s’ to denote the Dirac structures defined above. The factor of 2 comes from the fact that we can interchange the two currents. The pictorial representation of the two structures is given in the top row of Fig.(3). A further operator \tilde{Q} , corresponding the bottom two diagrams in Fig.(3) can be defined as

$$\tilde{Q} = (\bar{s}^i \gamma^\mu P_L d^l) (\bar{s}^k \gamma_\mu P_L d^j), \quad (3.2)$$

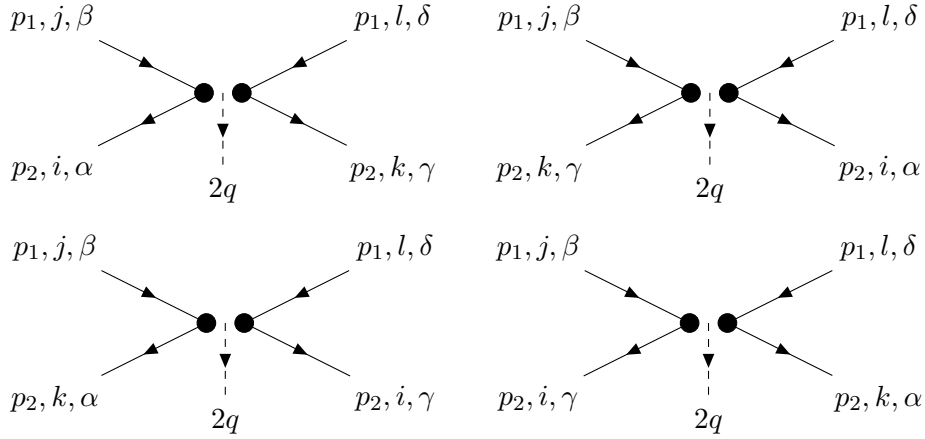


Figure 3. The four configurations of the external indices, corresponding to the following structures described in the text: $(\Gamma \otimes \Gamma \mathbb{1} \otimes \mathbb{1})$, $(\Gamma \tilde{\otimes} \Gamma \mathbb{1} \tilde{\otimes} \mathbb{1})$, $(\Gamma \otimes \Gamma \mathbb{1} \tilde{\otimes} \mathbb{1})$, $(\Gamma \tilde{\otimes} \Gamma \mathbb{1} \otimes \mathbb{1})$ (left to right, top to bottom). Each dot corresponds to an insertion of a current Γ and arrows indicate fermion and momentum flow.

with the matrix element given by

$$\langle \tilde{Q} \rangle = 2 Q^s \mathbb{1} \tilde{\otimes} \mathbb{1} - 2 \tilde{Q}^s \mathbb{1} \otimes \mathbb{1}. \quad (3.3)$$

The Greens functions $\langle \tilde{Q} \rangle$ differ from those of $\langle Q \rangle$ only by interchange of the two colour structures.

The expressions for the matrix elements can be split into two parts

$$\langle Q \rangle = \langle Q \rangle_1 + \langle Q \rangle_2, \quad (3.4)$$

where $\langle Q \rangle_1 = -2(\gamma^\mu P_L)_{\alpha\delta}(\gamma_\mu P_L)_{\gamma\beta} \delta^{il} \delta^{kj}$ and $\langle Q \rangle_2 = 2(\gamma^\mu P_L)_{\alpha\beta}(\gamma_\mu P_L)_{\gamma\delta} \delta^{ij} \delta^{kl}$. Next, we recall that our projectors, defined in Eqs.(2.6, 2.7) are of the form

$$P_{\alpha\beta,\gamma\delta} \propto X_{\beta\alpha} Y_{\delta\gamma} \delta_{ij} \delta_{kl}. \quad (3.5)$$

Projecting the two structures in Eq.(3.4) results in two types of spinor index contractions

$$P\langle Q \rangle_1 \propto \text{Tr}(X\gamma^\mu P_L Y\gamma_\mu P_L), \quad (3.6)$$

$$P\langle Q \rangle_2 \propto \text{Tr}(X\gamma^\mu P_L)\text{Tr}(Y\gamma_\mu P_L). \quad (3.7)$$

The same traces can be obtained for $\langle \tilde{Q} \rangle$, but with different colour contractions. We will be denoting the structures that result in double traces, like in Eq.(3.7) as “crossed”, corresponding to diagrams on the LHS of Figure 3. The structures that lead to single traced contractions as in Eq.(3.6) and the related diagrams on the RHS of Figure 3 we will call “direct”.

3.2 Bilinears and invariants

A complete set of bilinears can be chosen to be:

$$\not{p}_i P_L, \quad \gamma^\mu P_L, \quad \not{p}_1 \not{p}_2 \gamma^\mu P_L,$$

as in four dimensions any structure involving a bilinear of length three or more can be reduced to these three structures. Consequently, in D dimensions, any Dirac structure can be written as a linear combination of evanescent structures E_i^s and the following four structures

$$Q^s = \gamma^\mu P_L \otimes \gamma_\mu P_L,$$

$$M_{11}^s = \not{p}_1 P_L \otimes \not{p}_1 P_L, \quad M_{12}^s = \frac{1}{2} (\not{p}_1 P_L \otimes \not{p}_2 P_L + \not{p}_2 P_L \otimes \not{p}_1 P_L), \quad M_{22}^s = \not{p}_2 P_L \otimes \not{p}_2 P_L.$$

3.3 Matrix elements entering the total amplitude

Let us define the tree-level matrix elements, corresponding to the structures above, at generalised MOM kinematics as

$$\langle Q_1 \rangle = 2 Q^s 1 \otimes 1 - 2 \tilde{Q}^s 1 \tilde{\otimes} 1, \quad (3.8)$$

$$\langle Q_2 \rangle = 2 M_{11}^s 1 \otimes 1 - 2 \tilde{M}_{11}^s 1 \tilde{\otimes} 1, \quad (3.9)$$

$$\langle Q_3 \rangle = 2 M_{12}^s 1 \otimes 1 - 2 \tilde{M}_{12}^s 1 \tilde{\otimes} 1, \quad (3.10)$$

$$\langle Q_4 \rangle = 2 M_{22}^s 1 \otimes 1 - 2 \tilde{M}_{22}^s 1 \tilde{\otimes} 1, \quad (3.11)$$

We can also define the four further matrix elements $\langle \tilde{Q}_i \rangle$, $i = 1, \dots, 4$, with identical Lorentz structures but $\otimes \leftrightarrow \tilde{\otimes}$ for the colour contractions.

The total amplitude up to two loops can then be written in the form

$$\Lambda = \sum_{i=1}^4 (A_i \langle Q_i \rangle + \tilde{A}_i \langle \tilde{Q}_i \rangle) \quad (3.12)$$

+ linear combinations of evanescent Lorentz structures,

where A_i and \tilde{A}_i denote the coefficients in front of the tree-level matrix elements, obtained after reducing the structures appearing in the diagrams that make up the amplitude. The full set of diagrams contains both direct and crossed diagrams, such that the full Λ satisfies $\Lambda_{\alpha\beta\gamma\delta}^{ijkl} = -\Lambda_{\alpha\delta\gamma\beta}^{ilkj}$, as required by Fermi statistics, and accounted for by the form of $\langle Q_i \rangle$ and $\langle \tilde{Q}_i \rangle$.

3.4 Projectors and evanescent structures

When including all counterterm diagrams the coefficients are all finite, such that the projectors $P_{(i)}$ can be directly applied to Λ . However, we will not compute all the counterterms (renormalization constants) required to obtain finite coefficients for all the evanescent operators and therefore need a method of removing them in the presence of UV poles. In addition, we would like to use trace techniques to evaluate individual diagrams, which may be divergent. We are able to achieve both aims by choosing a set of projectors which are unambiguous in D dimensions and a set of evanescent operators which is projected to zero by all projectors.

We choose as projectors

$$\Pi_\mu(\Gamma_1 P_L \otimes \Gamma_2 P_L) = \text{tr } \gamma^\mu \Gamma_1 \gamma_\mu \Gamma_2, \quad (3.13)$$

$$\Pi_{11}(\Gamma_1 P_L \otimes \Gamma_2 P_L) = \text{tr } \not{p}_1 \Gamma_1 \not{p}_1 \Gamma_2, \quad (3.14)$$

$$\Pi_{12}(\Gamma_1 P_L \otimes \Gamma_2 P_L) = \text{tr } \not{p}_1 \Gamma_1 \not{p}_2 \Gamma_2, \quad (3.15)$$

$$\Pi_{22}(\Gamma_1 P_L \otimes \Gamma_2 P_L) = \text{tr } \not{p}_2 \Gamma_1 \not{p}_2 \Gamma_2, \quad (3.16)$$

with no trace over colour is understood. We have defined them only for the direct diagrams, specified earlier, because this is sufficient to reconstruct the entire result. To evaluate them, any chiral projector or γ_5 in any Dirac line should first be moved to the right end of that line. The traces are unambiguous in D dimensions because no Levi-Civita symbols are generated by them, nor by the tensor loop integrals we encounter.

We then define evanescent structures E_j^s such that $\Pi_i(E_j^s) = 0$ for all projectors Π_i as

$$E_1^s = \gamma^\mu \gamma^\nu \gamma^\rho P_L \otimes \gamma_\mu \gamma_\nu \gamma_\rho P_L - ((D-10)D + 8)Q^s, \quad (3.17)$$

$$E_3^s = \gamma^\mu \gamma^\nu \gamma^\rho \gamma^\sigma \gamma^\tau P_L \otimes \gamma_\mu \gamma_\nu \gamma_\rho \gamma_\sigma \gamma_\tau P_L - (D-2)(D((D-26)D + 152) - 128)Q^s, \quad (3.18)$$

$$F_{ij}^s = \frac{1}{2} (\not{p}_i \gamma^\mu \gamma^\nu P_L \otimes \not{p}_j \gamma_\mu \gamma_\nu P_L + (i \leftrightarrow j)) + (D-2)(D-4)M_{ij}^s - 4p_i \cdot p_j Q^s, \quad (3.19)$$

$$H_{ij}^s = \frac{1}{2} (\not{p}_i \gamma^\mu \gamma^\nu \gamma^\rho \gamma^\sigma P_L \otimes \gamma_\mu \gamma_\nu \gamma_\rho \gamma_\sigma \not{p}_j P_L + (i \leftrightarrow j)) - (D(D-14) + 32)(D-2)(D-4)M_{ij}^s + 8(D-8)(D-2)p_i \cdot p_j Q^s, \quad (3.20)$$

$$G_1^s = \frac{1}{2} (\not{p}_1 \not{p}_2 \gamma^\mu P_L \otimes \gamma_\mu P_L + \gamma^\mu P_L \otimes \not{p}_1 \not{p}_2 \gamma_\mu P_L) - p_1 \cdot p_2 Q^s, \quad (3.21)$$

$$G_2^s = \not{p}_1 \not{p}_2 \gamma^\mu \gamma^\nu \gamma^\rho P_L \otimes \not{p}_1 \not{p}_2 \gamma_\mu \gamma_\nu \gamma_\rho P_L - (D-4)(D(D-14) + 32) (p_2^2 M_{11}^s + p_1^2 M_{22}^s - 2p_1 \cdot p_2 M_{12}^s) + (D(D-10) + 8)p_1^2 p_2^2 Q^s, \quad (3.22)$$

$$G_3^s = \frac{1}{2} (\not{p}_1 \not{p}_2 \gamma^\mu \gamma^\nu \gamma^\rho P_L \otimes \gamma_\mu \gamma_\nu \gamma_\rho P_L + \gamma^\mu \gamma^\nu \gamma^\rho P_L \otimes \not{p}_1 \not{p}_2 \gamma_\mu \gamma_\nu \gamma_\rho P_L) + (D(D-10) + 8)p_1 \cdot p_2 Q^s, \quad (3.23)$$

$$G_4^s = \not{p}_1 \not{p}_2 \gamma^\mu P_L \otimes \not{p}_1 \not{p}_2 \gamma_\mu P_L + (D-4) (p_2^2 M_{11}^s + p_1^2 M_{22}^s - 2p_1 \cdot p_2 M_{12}^s) - p_1^2 p_2^2 Q^s. \quad (3.24)$$

All 12 evanescent structures (24 when including colour) are symmetric under the exchange of both bilinears and therefore (upon adding the piece required by Fermi symmetry) are the matrix elements of suitably chosen operators.

3.5 Obtaining coefficients A_i and \tilde{A}_i

As before, let us split $\langle Q_i \rangle = \langle Q_i \rangle_1 + \langle Q_i \rangle_2$, where $\langle Q_i \rangle_1$ denotes the second term on the r.h.s. of each of (3.8)–(3.11), which is due to the “direct” Feynman diagram. Moreover, we apply the same procedure to $\langle \tilde{Q}_i \rangle$. The entire amplitude Λ then splits in a similar manner

	Π_μ	Π_{11}	Π_{12}	Π_{22}
Q^s	$-2(D-2)D$	$-2(D-2)p_1^2$	$-2(D-2)(p_1 \cdot p_2)$	$-2(D-2)p_2^2$
M_{11}^s	$-2(D-2)p_1^2$	$2p_1^4$	$2p_1^2(p_1 \cdot p_2)$	$4(p_1 \cdot p_2)^2 - 2p_1^2p_2^2$
M_{12}^s	$-2(D-2)(p_1 \cdot p_2)$	$2p_1^2(p_1 \cdot p_2)$	$2p_1^2p_2^2$	$2p_2^2(p_1 \cdot p_2)$
M_{22}^s	$-2(D-2)p_2^2$	$4(p_1 \cdot p_2)^2 - 2p_1^2p_2^2$	$2p_2^2(p_1 \cdot p_2)$	$2p_2^2$

Table 1. $B_{ij} = \Pi_i Q_j^s$ for projectors, defined in Eqs.(2.6-2.7), and the structures, given in Sec.(3.2).

into a direct and a crossed contribution. The direct contribution is due to all the direct diagrams, and has the form

$$\Lambda_1 = \sum_{i=1}^4 (A_i \langle Q_i \rangle_1 + \tilde{A}_i \langle \tilde{Q}_i \rangle_1) \quad (3.25)$$

+ linear combinations of evanescent Lorentz structures.

Λ_1 enjoys the property that our projectors Π_i are defined on it, on a diagram-by-diagram basis. We can therefore compute

$$\begin{aligned} \Pi_i(\Lambda_1) &= \sum_{j=1}^4 \left(A_j \Pi_i(\langle Q_j \rangle_1) + \tilde{A}_j \Pi_i(\langle \tilde{Q}_j \rangle_1) \right) \\ &= \sum_{j=1}^4 B_{ij} \left(A_j 1 \tilde{\otimes} 1 + \tilde{A}_j 1 \otimes 1 \right) \\ &= \sum_{j=1}^4 \left(C_i 1 \tilde{\otimes} 1 + \tilde{C}_i 1 \otimes 1 \right), \end{aligned} \quad (3.26)$$

wherein contributions proportional to the tree-level matrix elements of the evanescent operators have disappeared, and the matrix B is readily found by applying the projectors Π_i to the basis Dirac structures Q^s , M_{11}^s , M_{12}^s and M_{22}^s . After summing over diagrams and counter-diagrams, we should find explicitly that C_i and \tilde{C}_i are finite, and can compute A_i and \tilde{A}_i via the inverse of B . B is nonsingular except for $q^2 = 0$; if we want a result directly at $q^2 = 0$ we need to redo the procedure with a subset of basis structures and a 2×2 B -matrix which then should be nonsingular.

Computation of the $B_{ij} = \Pi_i Q_j^s$ for our choice of projectors and operators is given in Table 1. One can make B dimensionless by rescaling the momentum-dependent basis structures and projectors by some scalar product(s) of momenta.

3.6 Obtaining the (S)MOM projections

Once the A_i and \tilde{A}_i are found, calculating the projections $P_{(\gamma_\mu)}(\Lambda)$ and $P_{(\not{g})}(\Lambda)$ (or any other projections) amounts to simply computing

$$P_{(i)}(\Lambda) = \sum_{j=1}^4 \left(\sum A_j P_{(i)}(\langle Q_j \rangle) + \sum \tilde{A}_j P_{(i)}(\langle \tilde{Q}_j \rangle) \right), \quad (3.27)$$

which is a $D = 4$ exercise. Here one needs to include both direct and crossed part and colour. The projections of the tree-level basis structures are given by

$$P_{(\gamma_\mu)}(\langle Q_i \rangle) = \left\{ \frac{1}{4} - \frac{3\epsilon}{16} + \frac{\epsilon^2}{32}, -\frac{\mu^2}{16} \left(1 - \frac{\epsilon}{4}\right), \frac{\mu^2}{32}(\omega - 2) \left(1 - \frac{\epsilon}{4}\right), -\frac{\mu^2}{16} \left(1 - \frac{\epsilon}{4}\right) \right\}, \quad (3.28)$$

$$P_{(\not{D})}(\langle Q_i \rangle) = \left\{ \frac{1}{4} - \frac{\epsilon}{16}, -\frac{\mu^2}{32}(\omega + 1), \frac{\mu^2}{64}(3\omega - 2), -\frac{\mu^2}{32}(\omega + 1) \right\}, \quad (3.29)$$

$$P_{(\gamma_\mu)}(\langle \tilde{Q}_i \rangle) = \left\{ \frac{1}{4} - \frac{5\epsilon}{16} + \frac{3\epsilon^2}{32}, -\frac{\mu^2}{16} \left(1 - \frac{3\epsilon}{4}\right), \frac{\mu^2}{32}(\omega - 2) \left(1 - \frac{3\epsilon}{4}\right), -\frac{\mu^2}{16} \left(1 - \frac{3\epsilon}{4}\right) \right\}, \quad (3.30)$$

$$P_{(\not{D})}(\langle \tilde{Q}_i \rangle) = \left\{ \frac{1}{4} - \frac{3\epsilon}{16}, \frac{\mu^2}{32}(\omega - 3), \frac{\mu^2}{64}(\omega - 6), \frac{\mu^2}{32}(\omega - 3) \right\}. \quad (3.31)$$

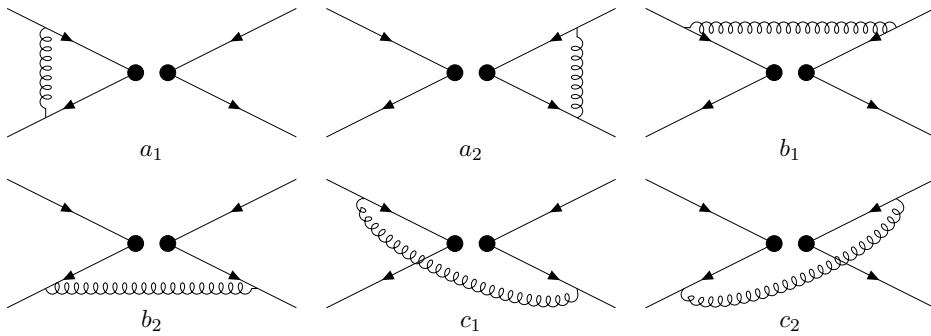
where $p_1^2 = p_2^2 = -\mu^2, q^2 = -\omega\mu^2$. For RI-MOM $\omega = 0$ and for RI-SMOM $\omega = 1$. These expressions are exact, i.e. they include all orders of ϵ .

4 Loop calculation

We proceed to discuss the calculation and present the results for two-loop kaon bag parameter. This section is organised as follows. In Section 4.1 we briefly discuss the one-loop amplitude. In Section 4.2 we review the diagrams that comprise the bare two-loop amputated Greens functions. As the two-loop calculation is much more involved, we give further details on how we define the topologies in Section 4.3 and evaluate the master integrals in Section 4.4, followed by the definition of renormalized amplitude in Section 4.6.

4.1 Amplitude at NLO

The one-loop amplitude can be obtained from the sum of the following 6 diagrams and their permutations of external legs (corresponding to Fig.(3)) and exchange of the two currents:



The computation of this amplitude can be found in [17], where it was done with open indices, by employing the Passarino-Veltmann technique and performing the projections in 4 dimensions. We will reproduce these results using our technique as part of the validation.

In order to obtain finite C_i and \tilde{C}_i we have to renormalize the amplitude Λ_1 . Renormalized amplitude is given by

$$\Lambda_{\text{ren}} = Z_q^2 (Z_{QQ} \langle Q \rangle + Z_{QE_n} \langle E_n \rangle), \quad (4.1)$$

where $\langle Q \rangle$ and $\langle E_n \rangle$ are the bare matrix elements, which can be expanded in α_s^{bare} as

$$\langle Q \rangle = \langle Q \rangle^{\text{tree}} + \frac{\alpha_s^{\text{bare}}}{4\pi} \langle Q \rangle^{1\text{-loop}} + \left(\frac{\alpha_s^{\text{bare}}}{4\pi} \right)^2 \langle Q \rangle^{2\text{-loop}}, \quad (4.2)$$

and similarly for $\langle E_n \rangle$. The one-loop renormalized amplitude is given by

$$\Lambda_{\text{ren}}^{(1)} = \langle Q \rangle^{1\text{-loop}} + (2Z_q^{(1)} + Z_{QQ}^{(1)}) \langle Q \rangle^{\text{tree}} + Z_{QE_F}^{(1)} \langle E_F \rangle^{\text{tree}}. \quad (4.3)$$

where $\langle Q \rangle^{1\text{-loop}}$ is the one-loop matrix element, obtained from the sum of the six diagrams and the wave function renormalization constant is given in Eq.(B.3). The rest of the evanescent operators do not enter this amplitude as by definition their tree-level matrix elements project to zero.

4.2 Amplitude at NNLO

The direct part of the two-loop amplitude is comprised of 103 diagrams. 36 of these are recursively one-loop, i.e. they involve insertions of self-energies into the propagators of one-loop diagrams. The remaining 67 diagrams are the true two-loop diagrams. In Figure 4 we give the pictorial representation of the unique 28 diagrams. The rest of the diagrams can be obtained by exchanging the external legs and the currents.

The final hurdles of this calculation involve computing the projected diagrams and obtaining the renormalized amplitude, which is finite in $D = 4$ dimensions. The general procedure for solving loop integrals involves first reducing them into a set of master integrals, which can then be evaluated. This is achieved using the integration by parts (IBP) method [18]. The procedure minimises the overall uncertainty of the amplitude. In the end we will find that all of the diagrams will reduce to around 30 masters. The resulting diagrams can then in principle be evaluated numerically, however it is always beneficial to use as many analytic results as there are available for better precision.

Once the amplitude is computed its poles have to cancel against the counterterms. The computation of counterterms themselves involves one-loop calculations as well as extractions of two-loop renormalization constants from the anomalous dimensions. All poles must cancel in the final result.

4.3 Defining two-loop topologies

As we perform projections first it is sufficient to consider scalar integrals. Thus, in this section we focus on the scalar part of our 4-point function $\Lambda_{\alpha\beta,\gamma\delta}^{ij,kl}$. At tree level, this amplitude can be pictured as shown in Figure 2: we have two particles with momentum p_1 going into the vertex and two particles with momentum p_2 , as well as $q = p_2 - p_1$, that ensures momentum conservation in the case of $p_1 \neq p_2$, going out of the vertex.

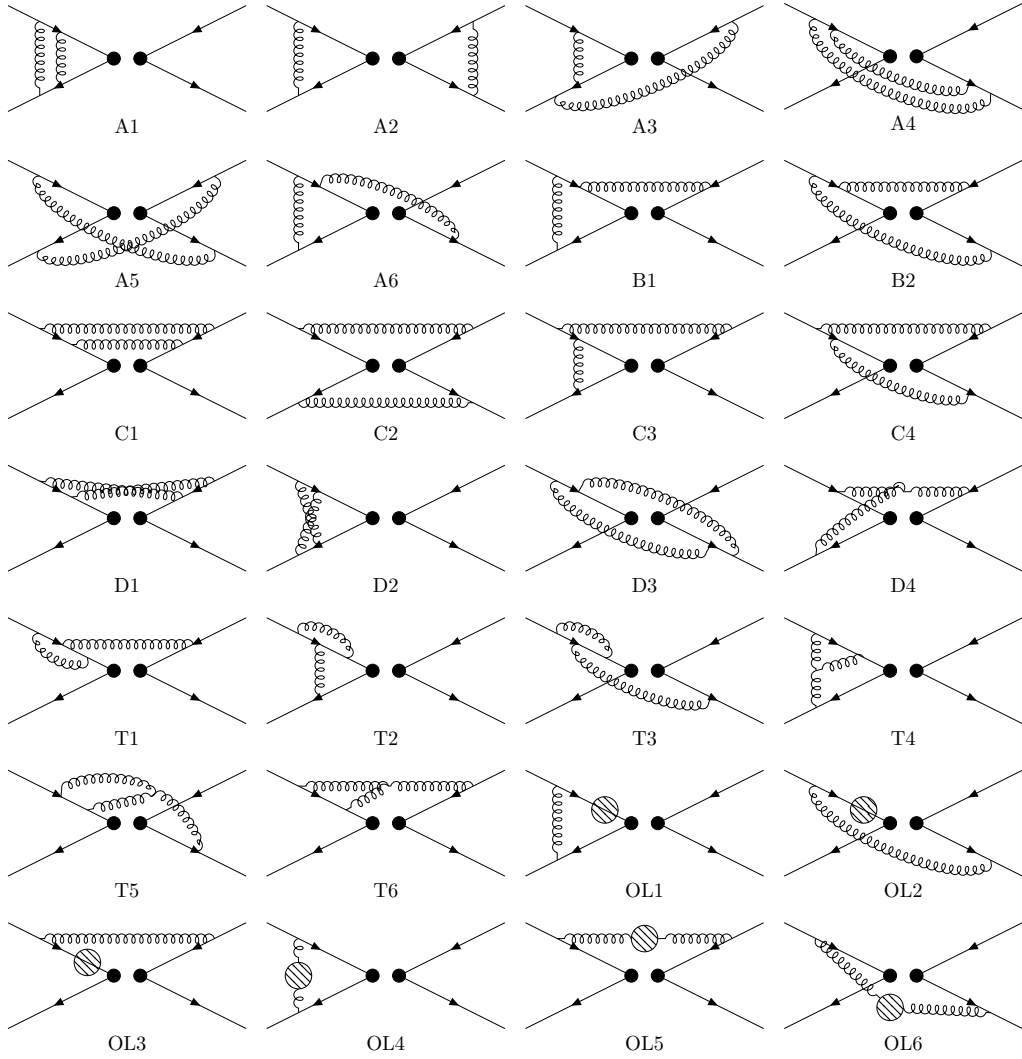


Figure 4. 28 classes of diagrams corresponding to the two-loop radiative corrections to the $\Lambda_{\alpha\beta,\gamma\delta}^{ij,kl}$. The hatched blobs correspond to the sum of one-loop insertions into the propagators. Kinematics are defined in Figure 2.

In order to compute the NNLO corrections for this diagram, we have to consider all of the possible two-loop radiative corrections, given in Figure 4. The diagrams can be divided into six groups: A, B, C, D, T and OL. Diagrams A, B and D correspond to the topologies with the same name. The diagrams C have linearly dependent propagators and can be written in terms of topologies A, B, C2 and C3. T stands for the remaining triangle integrals and OL for the integrals with one-loop insertions, both of which can be expressed in terms of topology A, B, C and D integrals. All of the topologies are shown in Figure 5 and the propagators are given in Table 2. Further details on the mapping of the integrals onto the topologies can be found in [19].

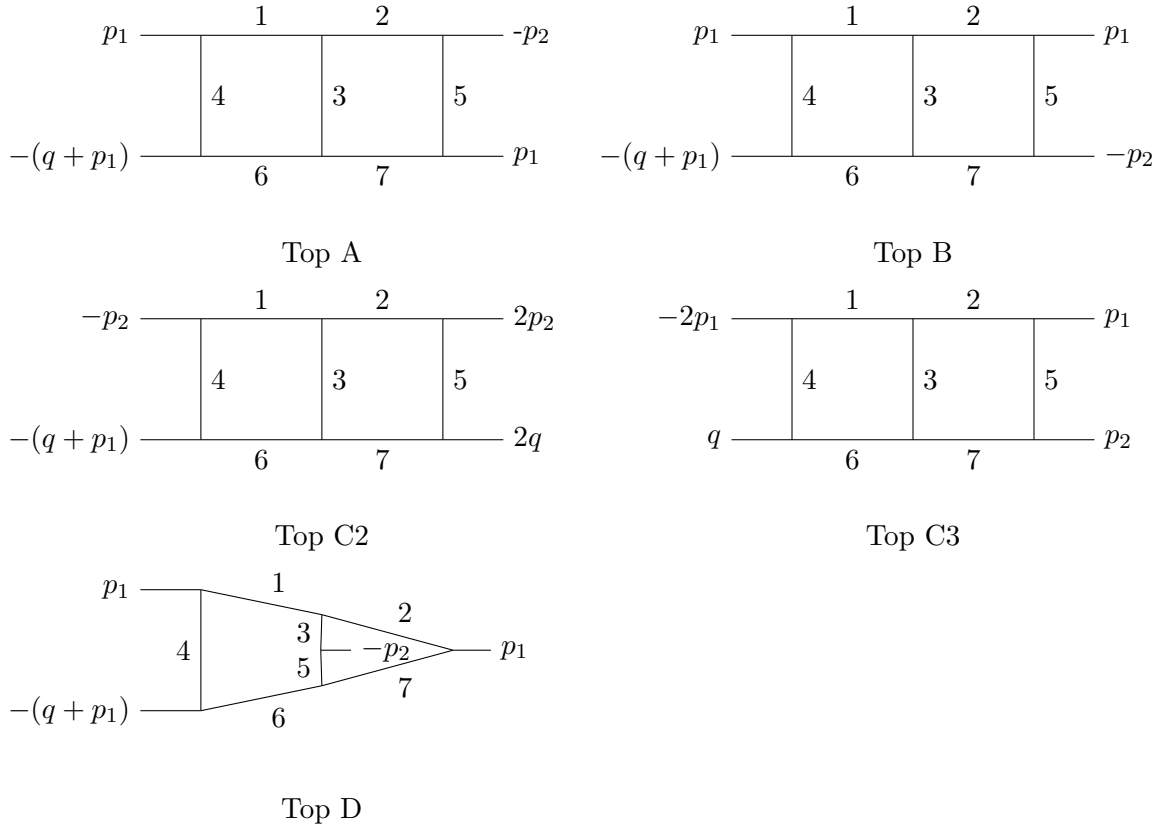


Figure 5. Topologies A, B, C2, C3 and D. All external momenta are defined as incoming. Numbers correspond to propagator labels, as defined in Section 4.3.

4.4 Master integrals and evaluation

After expressing all the integrals in terms of the five topologies we can proceed to calculate the IBP identities, using `Reduze 2` [20, 21]. This allows us to express the results in terms of a minimal set of master integrals. We find that our set contains 15 unique two-loop diagrams, shown in Figure 6.

The computation on the Lattice is done at a fixed renormalization scale, hence it is

	Top A	Top B	Top C2	Top C3	Top D
1.	k_1	k_1	k_1	k_1	k_1
2.	k_2	k_2	k_2	k_2	k_2
3.	$k_1 - k_2$	$k_1 - k_2$	$k_1 - k_2$	$k_1 - k_2$	$k_1 - k_2$
4.	$k_1 + p_1$	$k_1 - p_1$	$k_1 + p_2$	$k_1 + 2p_1$	$k_1 - p_1$
5.	$k_2 + p_2$	$k_2 + p_1$	$k_2 + 2p_2$	$k_2 + p_1$	$k_1 - k_2 - p_2$
6.	$k_1 - q$	$k_1 + q$	$k_1 + 2p_1$	$k_1 + p_1 + p_2$	$k_1 + q$
7.	$k_2 - q$	$k_2 + q$	$k_2 + 2p_1$	$k_2 + p_1 + p_2$	$k_2 + p_1$

Table 2. List of propagators for topologies in Figure 5. The numbers correspond to the numbering of propagators in the corresponding topology.

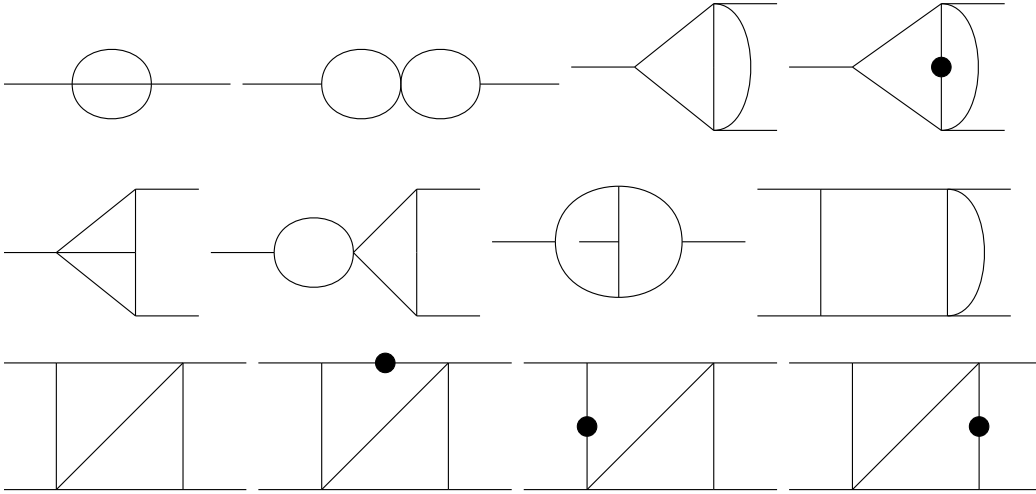


Figure 6. Two-loop master integrals. Black dots represent squared propagators.

sufficient to obtain the matching coefficient numerically at the corresponding scale. All of the necessary bubble diagrams are available up to any order in ϵ . The two-loop triangle diagrams have been calculated analytically up to finite order in the literature, whereas the results for the one-loop triangle are available to $\mathcal{O}(\epsilon)$ [22, 23]. In addition to these we also need the one-loop triangle up to $\mathcal{O}(\epsilon^2)$ for the one-loop matrix elements. There are no analytic results for the box diagrams with four off-shell legs available. We calculate the missing pieces and the box diagrams using sector decomposition method. We use PySecDec [24] to facilitate the evaluation of two-loop off-shell box diagrams as well as obtain the missing $\mathcal{O}(\epsilon)$ and $\mathcal{O}(\epsilon^2)$ of triangle diagrams. A more detailed discussion of the master integrals for the SMOM case can be found in [19].

4.5 Operators in Brod–Gorbahn basis

Our choice of evanescent operators differs from the ones used by J. Brod and M. Gorbahn (BG) [7] for the Wilson coefficients. The relevant operators are given by

$$E_1^{(2),\text{BG}} = (\bar{s}^i \gamma^{\mu_1 \mu_2 \mu_3 \mu_4 \mu_5} P_L d^j) (\bar{s}^k \gamma_{\mu_1 \mu_2 \mu_3 \mu_4 \mu_5} P_L d^l) - \left(256 - 224\epsilon - \frac{108\,816}{325} \epsilon^2 \right) Q,$$

$$E_2^{(2),\text{BG}} = (\bar{s}^i \gamma^{\mu_1 \mu_2 \mu_3 \mu_4 \mu_5} P_L d^l) (\bar{s}^k \gamma_{\mu_1 \mu_2 \mu_3 \mu_4 \mu_5} P_L d^j) - \left(256 - 224\epsilon - \frac{108\,816}{325} \epsilon^2 \right) (Q + E_F),$$

where $\gamma^{\mu_1 \mu_2 \dots} = \gamma^{\mu_1} \gamma^{\mu_2} \dots$. Comparing with Eq.(3.18), we can see that the difference is in the ϵ^2 parts of E_3 . Our choice of evanescent operators can be translated to the ones in which BG have obtained the NNLO Wilson coefficients and anomalous dimension matrices

as follows:

$$E_3 = E_1^{(2),\text{BG}} + \kappa \epsilon^2 Q, \quad (4.4)$$

$$E_4 = E_2^{(2),\text{BG}} + \kappa \epsilon^2 (Q + E_F), \quad (4.5)$$

where $\kappa = -62016/325$. As a result, the renormalized Green's functions of Q to NNLO differs between the two schemes as

$$\langle Q^{\overline{\text{MS}}} \rangle = \langle Q^{\overline{\text{MS}},\text{BG}} \rangle + \kappa Z_{QE_3}^{(2,2)} \langle Q \rangle^{\text{tree}} + \kappa Z_{QE_4}^{(2,2)} (\langle Q \rangle^{\text{tree}} + \langle E_F \rangle^{\text{tree}}), \quad (4.6)$$

with the Z factors given in App. E.

4.6 Renormalized amplitude

The renormalized two-loop amplitude can be written as

$$\begin{aligned} \Lambda_{\text{ren}}^{(2)} = & \langle Q \rangle^{2\text{-loop}} + 2Z_q^{(1)} \Lambda_{\text{ren}}^{(1)} + \left(Z_g^{(1)} + Z_\xi^{(1)} \xi \frac{\partial}{\partial \xi} + Z_{QQ}^{(1)} \right) \langle Q \rangle^{1\text{-loop}} \\ & + Z_{QE_n}^{(1)} \langle E_n \rangle^{1\text{-loop}} + (-3(Z_q^{(1)})^2 + 2Z_q^{(2)} + Z_{QQ}^{(2)}) \langle Q \rangle^{\text{tree}} + Z_{QE_n}^{(2)} \langle E_n \rangle^{\text{tree}}. \end{aligned} \quad (4.7)$$

where $n = \{F, 1, 2\}$. $\langle Q \rangle^{2\text{-loop}}$ is the two-loop matrix element, obtained from the sum of all diagrams, discussed in Section 4.2. $\Lambda_{\text{ren}}^{(1)}$ is the renormalized one-loop amplitude, defined in Eq.(4.3). $Z_{QQ}^{(1)}$ is the one-loop counterterm given in Eq.(D.2). The one- and two-loop wave function renormalization constants $Z_q^{(1)}$ and $Z_q^{(2)}$ are listed in Eq.(B.3). The gauge and gauge parameter Z -factors $Z_g^{(1)}$ and $Z_\xi^{(1)}$ are provided in Eqs.(B.4, B.5) respectively. Including the scheme change outlined in the previous section along with Z factors in Eqs.(E.8, E.9), the amplitude in the BG scheme is given by

$$\Lambda_{\text{ren}}^{\text{BG}(2)} = \Lambda_{\text{ren}}^{(2)} - \left(\left(\kappa Z_{QE_3}^{(2,2)} + \kappa Z_{QE_4}^{(2,2)} \right) \langle Q \rangle^{\text{tree}} + \kappa Z_{QE_4}^{(2,2)} \langle E_F \rangle^{\text{tree}} \right). \quad (4.8)$$

All of our RI-(S)MOM to $\overline{\text{MS}}$ conversion results in the following sections are presented for the BG $\overline{\text{MS}}$ scheme.

5 Results

We present our results for the two-loop conversion factors from RI-(S)MOM to the $\overline{\text{MS}}$ scheme in Section 5.1 along with an analytic expression for the coefficients at general MOM and $\overline{\text{MS}}$ renormalization scales. In Section 5.2 we present the formulas for obtaining $C_{B_K}^{S \rightarrow RGI}$ and study its residual scale dependence in the 3 and 4 flavour theories. In Section 5.3 we use our results for the conversion factors to obtain $B_K^{\overline{\text{MS}}}$ and \hat{B}_K and investigate the uncertainty due to unknown N³LO corrections. In Section 5.4 we discuss conversion between numbers of flavours for \hat{B}_K . In Section 5.5 we proceed to obtain our main result for \hat{B}_K by updating the current FLAG average. Finally, we update the value of ϵ_K in Section 5.6 and the bag coefficient for D mixing in Section 5.7.

5.1 $C_{B_K}^{(S)\text{MOM}\rightarrow\overline{\text{MS}}}$ up to NNLO

We present the conversion factors $C_{B_K}^{(S)\text{MOM}\rightarrow\overline{\text{MS}}}$ for matching between RI-(S)MOM schemes to BG $\overline{\text{MS}}$ scheme up to two-loop order computed at Landau gauge and $N_c = 3$. In deriving the conversion factors via Eqs.(2.9, 2.10), we take NLO coefficients of $C_q^{(\not{q})}$ and $C_q^{(\gamma_\mu)}$ from [17] and the NNLO coefficients from [25] (setting $C_A = N_c$, $T_F = 1/2$) and [26] (setting $w = 1$, $r = 1$). We compute the projected amplitudes $P_{(i)}(\Lambda)$, as outlined in Section 3, using the renormalized amplitudes defined in Section 4 together with the counterterms, given in Appendices D and E. Expanding the conversion factors in α_s while keeping the (S)MOM and $\overline{\text{MS}}$ renormalization scales general gives

$$C_{B_K}^{S\rightarrow\overline{\text{MS}}}(\mu, \nu) = 1 + \frac{\alpha_s(\nu)}{4\pi} [C_{B_K, \text{NLO}}^S - 4L(\mu, \nu)] + \frac{\alpha_s^2(\nu)}{16\pi^2} [C_{B_K, \text{NNLO}}^S + C_{B_K, \text{NLO}}^S L(\mu, \nu)(18 - \frac{3}{9}f) + L(\mu, \nu) \{ (7 - \frac{4}{9}f) - L(\mu, \nu)(72 - \frac{12}{9}f) \}] , \quad (5.1)$$

where S is the momentum subtraction scheme, $L(\mu, \nu) = \log(\nu/\mu)$, $\mu = \sqrt{-p^2}$ is the momentum subtraction scale, ν the dimensional scale, f the number of flavours, and $C_{B_K, \text{NLO}}^S$ and $C_{B_K, \text{NNLO}}^S$ are the NLO and NNLO coefficients of $C_{B_K}^{S\rightarrow\overline{\text{MS}}}$, values of which are presented in Table 3. The coefficients of the α_s expansion are independent of the momentum subtraction scale as is the fully analytic NLO result. However, we evaluate the NNLO coefficient in part numerically, and this depends on the ratio μ/ν (but not on the scales individually). In Table 3 we present numerical results for $\mu = \nu$, keeping the number of flavours f general, assuming all quarks are massless. In deriving the NLO results we have also checked that our method correctly reproduces the corresponding values in [17]. The main uncertainties in these results arise from the numerical evaluation of the integrals. We have checked that the coefficients of all of the poles in the NNLO calculation are consistent with zero within the uncertainties as well as with analytic expressions in [6], hence they have been dropped.

In Table 4 we present values for the LO+NLO and LO+NLO+NNLO conversion factors (LO=1), as well as the difference between the NNLO and NLO corrections at $\nu = \mu$, for $f = 3$. We use the world average of $\alpha_s(M_Z) = 0.1180 \pm 0.0009$ [27], which we evolve down to the scale $\nu = \mu = 3$ GeV using the 4-loop QCD β function and threshold corrections available in RunDec [28]. We find the perturbative series exhibits excellent convergence as the NNLO corrections give relative contributions below 4% for all schemes. For the (γ_μ, γ_μ) , (\not{q}, \not{q}) and RI-MOM schemes, the NNLO contributions are larger than the NLO ones. However, the relative NLO corrections to the series are smaller compared to the other two schemes, while the NNLO contributions are of comparable size. Hence, we do not consider the perturbative behaviour in these cases to be abnormal. The dominant uncertainties here come from the error on $\alpha_s(\mu)$ at both NLO and NNLO.

5.2 Conversion to the RGI bag factor

Next, from the conversion factors to the $\overline{\text{MS}}$ scheme we construct the conversion factors $C_{B_K}^{S \rightarrow \text{RGI}}$ to the scale- and scheme-independent bag factor \hat{B}_K , for any number of flavours f as

$$C_{B_K}^{S \rightarrow \text{RGI}} = U_{(f)}^{(0)}(\nu) \left(1 + \frac{\alpha_s^{(f)}(\nu)}{4\pi} J_{(f)}^{(1)} + \left(\frac{\alpha_s^{(f)}(\nu)}{4\pi} \right)^2 J_{(f)}^{(2)} \right) C_{B_K}^S(\nu), \quad (5.2)$$

where the relevant parts of the RG evolution operator [7] are given by

$$U_{(f)}^{(0)}(\nu) = (\alpha_s^{(f)}(\nu))^{-\frac{6}{33-2f}}, \quad (5.3)$$

$$J_{(f)}^{(1)} = \frac{2f(4f - 813) + 13\,095}{6(33 - 2f)^2}, \quad (5.4)$$

$$J_{(f)}^{(2)} = \frac{1}{2700(33 - 2f)^4} (-52\,000f^5 + 1\,755\,216f^4 + 33\,796\,944f^3 - 1\,897\,533\,864f^2 + 25\,597\,290\,654f - 119\,065\,711\,779 - 21\,600(2f - 33)^2(5f + 63)\zeta(3)). \quad (5.5)$$

The $C_{B_K}^{S \rightarrow \text{RGI}}$ are formally independent of the $\overline{\text{MS}}$ scale ν . Their residual scale dependence for the 3 and 4 flavour scenarios for the most commonly used MOM schemes is presented in Figures 7 and 8 for momentum subtraction scales $\mu = 3$ GeV ($f = 3$) and $\mu = 5$ GeV ($f = 4$) respectively. We can see that the (\not{q}, \not{q}) scheme exhibits the best behaviour in terms of perturbative convergence as well as the size of the residual scale dependence. While RI-MOM schemes are the same at NLO, RI'-MOM scheme converges better at NNLO. Comparing Figures 7 and 8 we can see a further improvement in the convergence of the perturbative series as well as further reduction in the scale dependence for the 4 flavour $\mu = 5$ GeV case. In addition, in Table 5 we present numerical values for $C_{B_K}^{S \rightarrow \text{RGI}}$ for $\mu = 3$ GeV, including the ratios of the uncertainties coming from α_s versus residual scale variation. It is clear that in each case the uncertainty due to scale variation dominates.

S	$C_{B_K, \text{NLO}}^S$	$C_{B_K, \text{NNLO}}^S$
(γ_μ, \not{q})	$8 \log 2 - 8 = -2.45482\dots$	$3.88f + 21.05 \pm 0.08$
(γ_μ, γ_μ)	$8 \log 2 - 16/3 = 0.211844\dots$	$-0.42f + 86.41 \pm 0.08$
(\not{q}, \not{q})	$8 \log 2 - 6 = -0.454823\dots$	$0.90f + 52.78 \pm 0.09$
(\not{q}, γ_μ)	$8 \log 2 - 10/3 = 2.21184\dots$	$-3.39f + 123.47 \pm 0.09$
RI'-MOM	$8 \log 2 - 14/3 = 0.878511\dots$	$0.17f + 61.71 \pm 0.07$
RI-MOM	$8 \log 2 - 14/3 = 0.878511\dots$	$-4.49f + 94.04 \pm 0.07$

Table 3. $C_{B_K, \text{NLO}}^S$ and $C_{B_K, \text{NNLO}}^S$ as defined in Eq.(5.1). The values presented are in Landau gauge with $N_c = 3$ and the NNLO result computed at $\nu = \mu = \sqrt{-p^2}$ for two RI-MOM schemes ($S = \{\text{RI-MOM}, \text{RI'-MOM}\}$) and four RI-SMOM schemes ($S = (X, Y)$ with $X = \gamma_\mu, \not{q}$ and $Y = \gamma_\mu, \not{q}$). The uncertainty in these results arises due to in-part numerical evaluation of the two-loop integrals.

S	NLO	NNLO	diff.
(γ_μ, \not{q})	0.9523(8)	0.9646(4)	0.0124(9)
(γ_μ, γ_μ)	1.00412(7)	1.036(1)	0.032(1)
(\not{q}, \not{q})	0.9912(1)	1.0121(6)	0.0210(6)
(\not{q}, γ_μ)	1.0430(7)	1.086(2)	0.043(2)
RI'-MOM	1.0171(3)	1.041(1)	0.024(1)
RI-MOM	1.0171(3)	1.048(1)	0.030(1)

Table 4. Conversion factors $C_{B_K}^S$ evaluated with $\alpha_s(\mu)$ including NLO (i.e. 1+NLO) and NNLO (i.e. 1+NLO+NNLO) corrections, as well as the difference |diff. | between the two (i.e. NNLO) in Landau gauge for RI-MOM schemes ($S = \{\text{RI-MOM}, \text{RI}'\text{-MOM}\}$) and four RI-SMOM schemes ($S = (X, Y)$) with $X = \gamma_\mu, \not{q}$ and $Y = \gamma_\mu, \not{q}$. The results are computed at $\nu = \mu = \sqrt{-p^2} = 3$ GeV with $N_c = 3$ and $f = 3$. The dominant uncertainty in these results is due to the error on $\alpha_s(3 \text{ GeV})$.

5.3 $B_K^{\overline{\text{MS}}}$, \hat{B}_K and their residual scale dependence

Taking our results for the conversion factors we can perform a matching calculation at 3 and 4 flavours as well as fixed momentum subtraction scale μ from the currently available lattice estimates of B_K [29–32]. We quote the lattice inputs and present our computed values of $B_K^{\overline{\text{MS}}}$ using one-loop and two-loop matching in Table 6, for $\nu = \mu$. We can see that inclusion of perturbative corrections leave the uncertainties comparable to the initial errors obtained on the lattice, meaning that the results so far are dominated by the lattice errors.

As $B_K^{\overline{\text{MS}}}(\nu)$ is not formally scale-invariant, we estimate the error due to uncomputed

S	NLO	$(\delta_{\alpha_s}/\delta_\nu)$	NNLO	$(\delta_{\alpha_s}/\delta_\nu)$
(γ_μ, \not{q})	1.35(3)	0.15	1.360(9)	0.62
(γ_μ, γ_μ)	1.42(2)	0.28	1.46(1)	0.22
(\not{q}, \not{q})	1.41(2)	0.23	1.428(9)	0.49
(\not{q}, γ_μ)	1.48(1)	0.31	1.53(2)	0.09
RI'-MOM	1.44(1)	0.39	1.47(1)	0.33
RI-MOM	1.44(1)	0.39	1.48(1)	0.22

Table 5. The NLO and NNLO conversion factors $C_{B_K}^{S \rightarrow \text{RGI}}$ in Landau gauge for RI-MOM schemes ($S = \{\text{RI-MOM}, \text{RI}'\text{-MOM}\}$) and four RI-SMOM schemes ($S = (X, Y)$) with $X = \gamma_\mu, \not{q}$ and $Y = \gamma_\mu, \not{q}$ computed at $\mu = \sqrt{-p^2} = 3$ GeV with $N_c = 3$ and $f = 3$, with ν varied from 2 to 6 GeV (central value of 3 GeV). The uncertainties include the error on α_s , and residual ν -dependence, where $(\delta_{\alpha_s}/\delta_\nu)$ indicates the ratio of the aforementioned uncertainties at NLO and NNLO for each scheme choice. The dominant errors in these results arise from the variation of the renormalization scale.

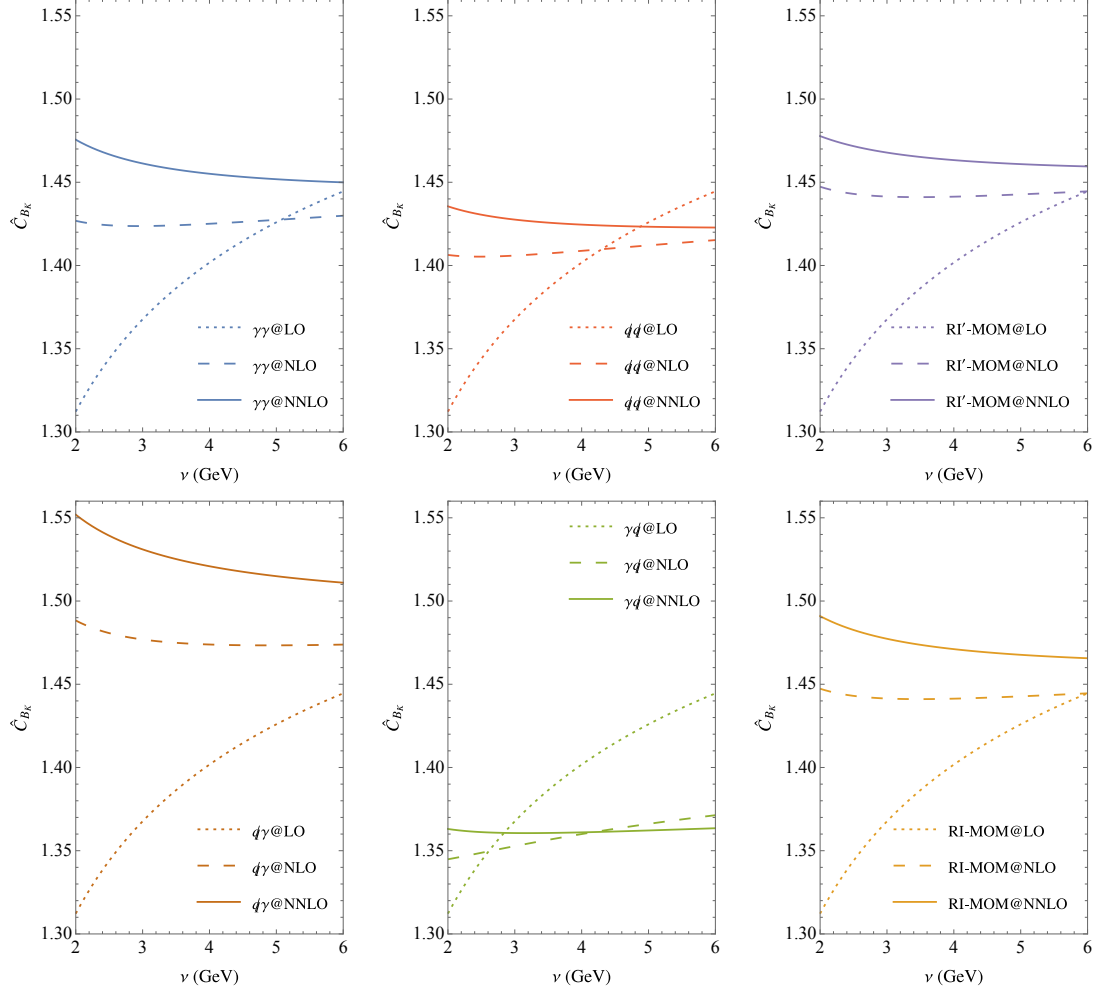


Figure 7. Conversion factors from RI-(S)MOM schemes to RGI for $\mu = 3$ GeV and $f = 3$.

Scheme	Lattice	NLO	NNLO	$\mu = \nu$	f
SMOM(\not{q}, \not{q})	0.5342(21)	0.5295(21)	0.5407(21)	3 GeV	3
SMOM(γ_μ, γ_μ)	0.5164(18)	0.5185(18)	0.5352(20)	3 GeV	3
RI-MOM ₁₆	0.517(13)	0.526(13)	0.542(14)	3 GeV	3
RI-MOM ₁₁	0.5308(61)	0.5393(62)	0.5536(64)	3.5 GeV	3
RI'-MOM	0.498(16)	0.507(16)	0.519(17)	3 GeV	4

Table 6. Bag parameter $B_K^{\overline{\text{MS}}}$ for the available $f = 3$ and $f = 4$ lattice inputs. Lattice results are taken from [29–32], where RI-MOM₁₆ corresponds to RBC/UKQCD 16 and RI-MOM₁₁ to BMW 11 results. The dominant uncertainties here are due to errors on the lattice results. Uncertainties due to higher-order perturbative corrections are not included in this Table.

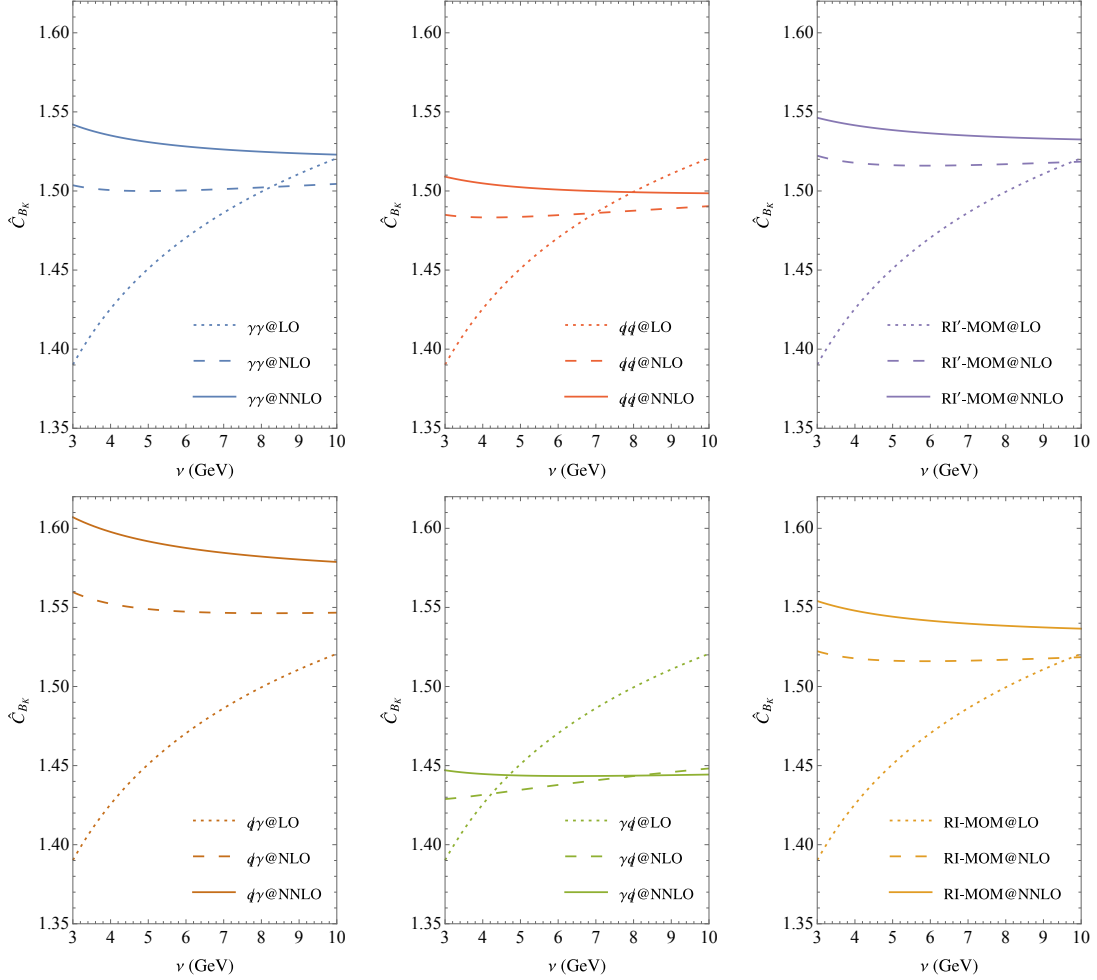


Figure 8. Conversion factors from RI-(S)MOM schemes to RGI for $\mu = 5$ GeV and $f = 4$.

higher orders as follows: We use our fixed-order conversion for a range $\nu \in [2, 6]$ GeV and $\overline{\text{MS}}$ -evolve it back to the scale $\nu = \mu$. The resulting variation gives us an estimate of the uncomputed higher orders. The results are given in Figure 9. As we can see the uncertainties associated with the SMOM schemes are significantly lower compared to MOM results, for which the residual scale dependence is fairly negligible compared to lattice errors. For SMOM schemes, on the other hand, the residual scale dependence is significant. One can also observe a nice overlap of the RBC/UKQCD results as opposed to the BMW 11 result, which gives a larger prediction for B_K albeit at a slightly higher scale μ .

We compute the RG-invariant value of the kaon bag parameter \hat{B}_K using the conversion factors in Eq.(5.2) along with the aforementioned Lattice results. The residual scale dependence of \hat{B}_K for the five lattice results is given in Figure 10. Again we see that the RBC/UKQCD results overlap nicely and the BMW 11 result lies above. Taking into account the scale variation, the two SMOM schemes agree with each other as well. As the ETM result is at 4 flavours it still can't be directly compared to the 3-flavour results,

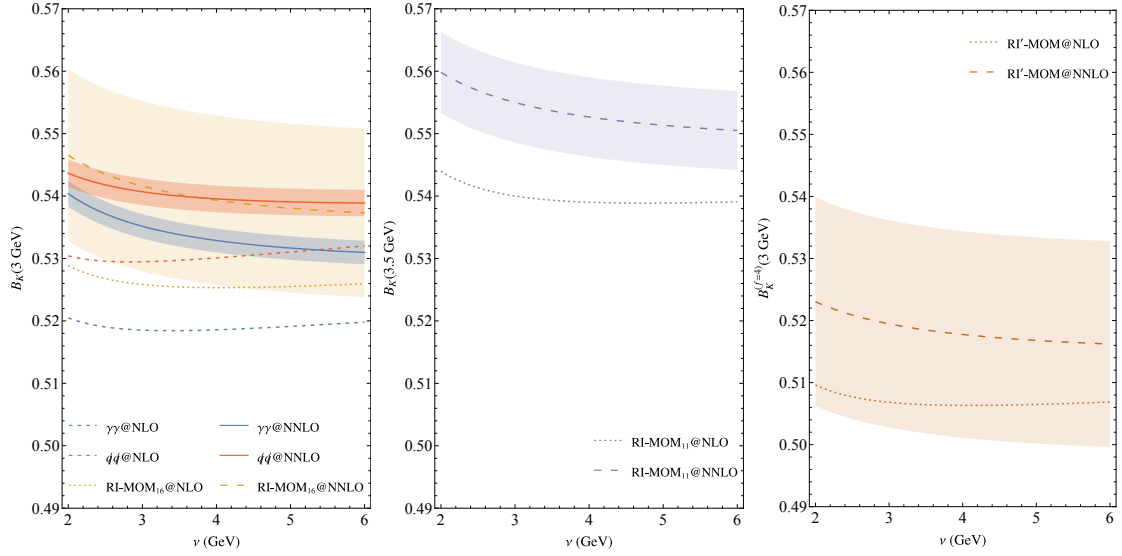


Figure 9. B_K in the BG $\overline{\text{MS}}$ scheme evaluated at 3 GeV ($f=3$, left), 3.5 GeV ($f=3$, middle) and at 3 GeV ($f=4$, right) as a function of the $\overline{\text{MS}}$ renormalization scale ν in Landau gauge for the two RI-SMOM schemes $\gamma\gamma$ and qq , RI-MOM and RI'-MOM. (For explanation, see text). The bands indicate the corresponding maximum and minimum values of B_K given the uncertainties on α_s , $C_{B_K, \text{NNLO}}$ and $B_K(\text{RI-(S)MOM}) = B_K^{\text{lat}}$. Here $\gamma\gamma$ and qq corresponds to B_K^{lat} from RBC/UKQCD 24 [29], RI-MOM₁₆ - B_K^{lat} from RBC/UKQCD 16 [30], RI-MOM₁₁ - B_K^{lat} from BMW 11 [31], RI'-MOM - B_K^{lat} from ETM 15 [32].

however as for the RI-MOM schemes we observe that residual scale variation introduces only a sub-dominant uncertainty.

5.4 Matching between number of flavours

In this section, we define a matching coefficient $\hat{M}^{(f \rightarrow f-1)}$ for obtaining the $\hat{B}_K^{(f)}$ from $\hat{B}_K^{(f-1)}$, i.e.

$$\hat{B}_K^{(f)} = \hat{M}^{(f \rightarrow f-1)} \hat{B}_K^{(f-1)}, \quad (5.6)$$

where f is the number of active flavours.

We extract $\hat{M}^{(f \rightarrow f-1)}$ from the results in [7] and obtain

$$\begin{aligned} \hat{M}^{(f \rightarrow f-1)} = & \frac{U_{(f)}^{(0)}(\nu)}{U_{(f-1)}^{(0)}(\nu)} \left(1 + \frac{\alpha_s^{(f-1)}(\nu)}{4\pi} (J_{(f)}^{(1)} - J_{(f-1)}^{(1)}) \right. \\ & + \left(\frac{\alpha_s^{(f-1)}(\nu)}{4\pi} \right)^2 \left(J_{(f)}^{(2)} - J_{(f-1)}^{(2)} - J_{(f-1)}^{(1)} (J_{(f)}^{(1)} - J_{(f-1)}^{(1)}) \right. \\ & \left. \left. + \frac{2}{3} J_{(f)}^{(1)} \log \frac{\nu^2}{m_f^2(\nu)} - \frac{2}{3} \log^2 \frac{\nu^2}{m_f^2(\nu)} - \frac{2}{9} \log \frac{\nu^2}{m_f^2(\nu)} - \frac{59}{54} \right) \right), \end{aligned} \quad (5.7)$$

where the relevant parts of the evolution kernel are defined in Eqs.(5.3, 5.4 and 5.5). In addition to the running of the matrix element, this expression also takes into account

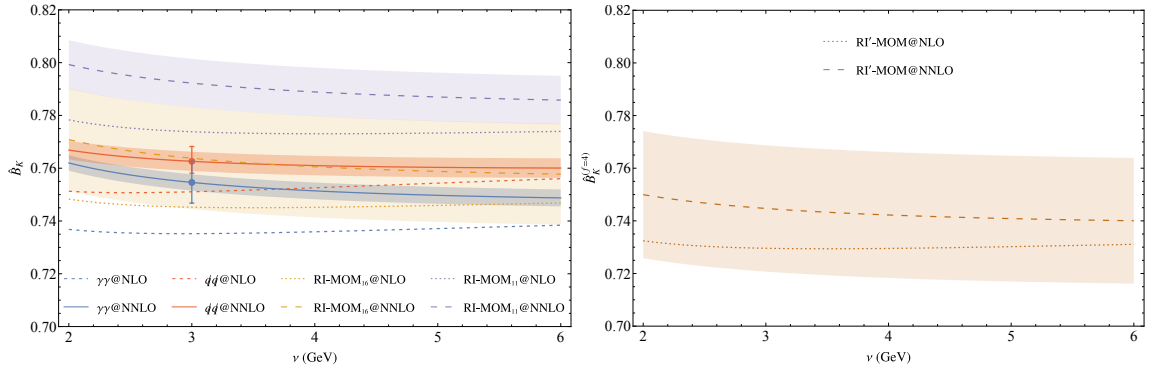


Figure 10. Residual dependence of \hat{B}_K on $\overline{\text{MS}}$ renormalization scale in Landau gauge for the two RI/SMOM schemes $\gamma\gamma$ and qq and RI-MOM at 3 flavours (left) and 4 flavours (right). The bands indicate the corresponding maximum and minimum values of \hat{B}_K given the uncertainties on α_s , $C_{B_K, \text{NNLO}}$ and $B_K^{\text{RI-(S)MOM}} = B_K^{\text{lat}}$. The error bars for $\gamma\gamma$ and qq also include the uncertainty due to the scale variation. Here $\gamma\gamma$ and qq corresponds to B_K^{lat} from RBC/UKQCD 24 [29], RI-MOM₁₆ - B_K^{lat} from RBC/UKQCD 16 [30], RI-MOM₁₁ - B_K^{lat} from BMW 11 [31], RI'-MOM - B_K^{lat} from ETM 15 [32].

threshold corrections associated with the change in flavours. One can see that $\hat{M}^{(f \rightarrow f-1)}$ is independent of the renormalization scale up to 2-loop order by taking a derivative with respect to ν . Using Eq.(5.7) along with 3-loop $\alpha_s(\nu)$ and $m_c(\nu)$ running we can plot the residual scale dependence of $\hat{M}^{(4 \rightarrow 3)}$, as shown in Figure 11. We observe excellent behaviour as the residual scale dependence is significantly smaller than the error from $\alpha_s(\nu)$.

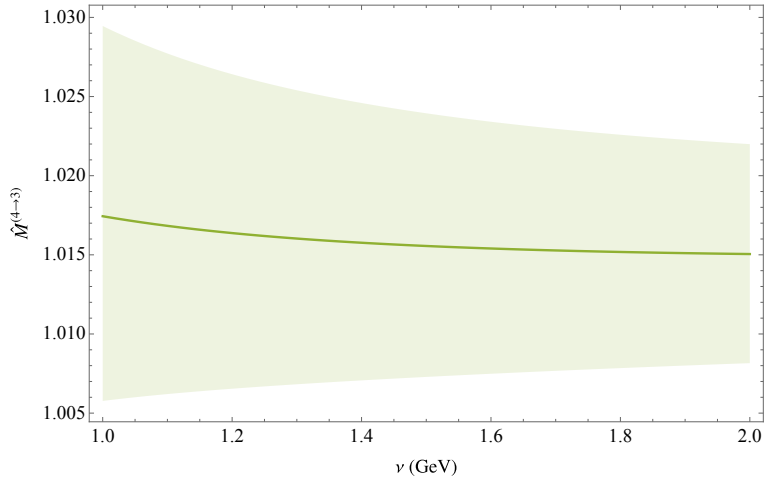


Figure 11. Dependence of $\hat{M}^{(4 \rightarrow 3)}$ on the $\overline{\text{MS}}$ renormalization scale. The bands indicate the corresponding maximum and minimum values of \hat{M} given the uncertainties on $\alpha_s(\nu_f)$ at 3 and 4 flavour.

f	Ref.	Scheme	μ (GeV)	$B_K^{(\text{Scheme})}(\mu)$	$\hat{B}_{K,\text{NLO}}^{(f)}$
4	ETM 15	RI'-MOM	3	0.498(16)	0.717(24)
3	RBC/	(\not{q}, \not{q})	3	0.5342(21)	0.7436(82)
	UKQCD 24	(γ_μ, γ_μ)	3	0.5164(18)	-
3	SWME 15A	$\overline{\text{MS}}$	3	0.519(26)	0.735(36)
3	RBC/	(\not{q}, \not{q})	3	0.5341(18)	0.7499(152)
	UKQCD 14B	(γ_μ, γ_μ)	3	0.5166(18)	-
3	Laiho 11	$\overline{\text{MS}}$	2	0.5572(152)	0.7628(208)
3	BMW 11	RI-MOM	3.5	0.5308(61)	0.7727(117)

Table 7. Summary of lattice results entering the current FLAG average [29, 31–35]. The $B_K^{(\text{Scheme})}(\mu)$ is taken from the corresponding literature and $\hat{B}_{K,\text{NLO}}^{(f)}$ from FLAG review [13].

5.5 \hat{B}_K global average

We proceed to compute the global averages of \hat{B}_K using our two-loop conversion. In Table 7 we review the existing results entering into the current 3 and 4 flavour FLAG averages. In Table 8 we present our updated values for the corresponding \hat{B}_K values in Table 7. Here we have also converted the 3 flavour results to 4 flavours and 4 flavour ETM 15 result to 3 flavours using Eq.(5.7).

To obtain the averages, we follow the procedure for averaging correlated data outlined by Schmelling [36]. As we expect the two results of RBC/UKQCD 24 [29] to be correlated

f	Ref.	Scheme	$\hat{B}_K^{(f=3)}$	$\hat{B}_K^{(f=4)}$
4	ETM 15	RI'-MOM	0.733(26)	0.745(25)
3	RBC/	(\not{q}, \not{q})	0.7626(56)	0.7749(93)
	UKQCD 24	(γ_μ, γ_μ)	0.7546(80)	0.767(11)
3	SWME 15A	$\overline{\text{MS}}$	0.735(36)*	0.747(37)
3	Laiho 11	$\overline{\text{MS}}$	0.7628(208)*	0.7751(224)
3	BMW 11	RI-MOM	0.790(13)	0.804(15)

Table 8. Summary of our updated results for \hat{B}_K . For $B_K^{(\text{Scheme})}(\mu)$ values given in MOM schemes (see Table 7) we obtain \hat{B}_K via two-loop matching to $\overline{\text{MS}}$ at $\nu = \mu$ and conversion to RGI value. The RGI errors take into account uncertainties in the lattice value, α_s , $C_{B_K}^S$ and $\overline{\text{MS}}$ residual scale variation. The asterisk (*) indicates that $\hat{B}_K^{(f=3)}$ is obtained from $\overline{\text{MS}}$ value using the conversion factor 1.369 as in [13]. The 3 flavour \hat{B}_K results are converted to 4 flavours and vice versa via Eq.(5.7).

we compute the full covariance matrix giving

$$f = 2 + 1 : \quad \hat{B}_K = 0.7600(53), \quad (\text{RBC/UKQCD 24 updated}) \quad (5.8)$$

where we use $\chi^2 = 0.671$ to estimate the size of the correlation to be 33.9%. The error is then simply taken to be the square root of the variance. Unlike FLAG review [13] we do not include the RBC/UKQCD 14B [34] result in the average as the newer result is a reanalysis of the same lattice measurement as the older one with an improved renormalization.

Next, we combine the results from SWME 15A [33], RBC/UKQCD 24 [29] Eq.(5.8), Laiho 11 [35] and BMW 11 [31]. Here and in the following we neglect correlations between different Lattice results, and get

$$f = 2 + 1 : \quad \hat{B}_K = 0.7637(62), \quad (5.9)$$

with $\chi^2/\text{dof} = 1.739$. According to our procedure, we rescale the error by square root of χ^2/dof . This result can be compared to the FLAG average of $\hat{B}_K = 0.7533(91)$ [13], which includes specific correlations between Lattice results. The $f = 2 + 1 + 1$ average is simply given by the 4 flavour ETM 15 [32] result, i.e.

$$f = 2 + 1 + 1 : \quad \hat{B}_K = 0.745(25), \quad (5.10)$$

which can again be compared to the FLAG average of $\hat{B}_K = 0.717(24)$ [13].

Furthermore, we use our results in Table 8 to obtain the full 3 and 4 flavour averages for \hat{B}_K using combined 3 and 4 flavour results. For 3 flavours we get

$$\hat{B}_K^{(f=3)} = 0.7627(60), \quad (5.11)$$

with $\chi^2/\text{dof} = 1.641$. Here, we also rescale the error by square root of χ^2/dof . For 4 flavours we once more compute the average of RBC/UKQCD 24 values $(\hat{B}_K^{(f=4)})_{\text{RBC/UKQCD}} = 0.7715(92)$ with correlation of 68.2%, followed by our full 4 flavour result

$$\hat{B}_K^{(f=4)} = 0.7759(84), \quad (5.12)$$

with $\chi^2/\text{dof} = 1.470$. Here, the error is also rescaled by square root of χ^2/dof .

5.6 ϵ_K updated value

Using our updated results for \hat{B}_K in Eq.(5.11) we can obtain an updated value for ϵ_K . As we observe a small shift in central value and reduction in error, we update the result of [10] by recomputing the non-perturbative contribution and get

$$|\epsilon_K| = 2.171(65)_{\text{pert.}}(71)_{\text{non-pert.}}(153)_{\text{param.}} \times 10^{-3}, \quad (5.13)$$

where the errors refer to perturbative, non-perturbative and parametric. As we can see our result leads to reduction of non-perturbative uncertainty from 3.5% to roughly 3.28%.

5.7 D meson mixing

One can also use our results for conversion factors to obtain the $\overline{\text{MS}}$ and RGI values of the D meson bag parameter computed by ETM 15 [32]. The results are summarized in Table 9.

Scheme	Lattice	NLO	NNLO	$\hat{B}_D^{(f=3)}$	$\hat{B}_D^{(f=4)}$
$B_D^{(f=4)}$ (RI'-MOM)	0.744(27)	0.757(27)	0.776(28)	1.095(41)	1.113(41)

Table 9. Bag parameter for D meson mixing. The Lattice value taken from ETM 15 [32]. The $\overline{\text{MS}}$ and RGI values computed analogously to B_K . The errors take into account uncertainties in the Lattice value, α_s and $C_{B_D}^S = C_{B_K}^S$. The RGI value errors also include $\overline{\text{MS}}$ residual scale variation.

6 Conclusions

Meson–anti-meson mixing plays a central role in current particle physics phenomenology, with the CP-violating parameter ε_K imposing very tight constraints on physics beyond the Standard Model. The theoretical predictions for these observables rely heavily on non-perturbative bag parameters, which must be converted from lattice renormalization schemes to the $\overline{\text{MS}}$ scheme to ensure compatibility with phenomenological analyses.

In this work, we derived the scheme conversion factors for several MOM and SMOM renormalization schemes at NNLO in QCD, verifying and extending the previously established NLO results. These NNLO conversion factors are essential for achieving precision in the determination of the bag parameter \hat{B}_K , a critical component of the ε_K calculation. We confirmed the numerical stability of our results, with residual scale dependence providing an estimate of potential higher-order corrections.

We calculated \hat{B}_K at NNLO for three and four active flavours, incorporating diverse lattice inputs that employed different non-perturbative renormalization schemes. By combining these inputs, we derived a new world average for \hat{B}_K at NNLO. The improved scheme conversion factors resulted in a more concise fit of the three-flavour \hat{B}_K enhancing both precision and consistency. Notably, our analysis included, for the first time, the perturbative matching of the charm-quark contribution to \hat{B}_K at $\mathcal{O}(\alpha_s^2)$, enabling a unified treatment of three- and four-flavour results.

The updated central value of \hat{B}_K , with a 1% shift and a reduced uncertainty of under 0.8%, represents a significant improvement. This enhanced precision will play a pivotal role in future phenomenological applications, further constraining the Standard Model and probing new physics scenarios.

Acknowledgments

The work of MG is partially supported by the UK Science and Technology Facilities Council grant ST/X000699/1. The work of SK has been funded by the European Union NextGenerationEU/PRTR under grant CNS2022-136024 and by MICIU/AEI/10.13039/501100011033 and FEDER/UE (grant PID2022-139466NB-C21). The work of SJ is supported in part by the UK Science and Technology Facilities Council grant ST/X000796/1.

A Fierz-evanescent operators

One can present the results in a slightly different manner, by trading the \tilde{Q}_i for Fierz-evanescent operators such that only a minimal number of operators contribute to the

renormalized Green's function at $D \rightarrow 4$ (and hence to the SMOM projections). We find that the following operators are evanescent, including the first one which we already had:

$$E_{1F} = \tilde{Q}_1 - Q_1, \quad (\text{A.1})$$

$$E_{2F} = Q_2 + \tilde{Q}_2 - \frac{p_1^2}{2}(Q_1 + E_{1F}), \quad (\text{A.2})$$

$$E_{3F} = Q_3 + \tilde{Q}_3 - \frac{p_1 \cdot p_2}{2}(Q_1 + E_{1F}), \quad (\text{A.3})$$

$$E_{4F} = Q_4 + \tilde{Q}_4 - \frac{p_2^2}{2}(Q_1 + E_{1F}). \quad (\text{A.4})$$

One can then rearrange e.g. Eq.(3.12) in terms of the (direct parts of the) matrix elements of Q_i and E_{iF} , which gives the new coefficients

$$A'_1 = A_1 + \tilde{A}_1 + \frac{p_1^2}{2}\tilde{A}_2 + \frac{p_1 \cdot p_2}{2}\tilde{A}_3 + \frac{p_2^2}{2}\tilde{A}_4, \quad (\text{A.5})$$

$$A'_2 = A_2 - \tilde{A}_2, \quad (\text{A.6})$$

$$A'_3 = A_3 - \tilde{A}_3, \quad (\text{A.7})$$

$$A'_4 = A_4 - \tilde{A}_4. \quad (\text{A.8})$$

The second sum in Eq.(3.27) then disappears without replacement, as the evanescent operators have zero tree-level matrix elements. Both methods give the same result.

B $\overline{\text{MS}}$ renormalization constants

$\overline{\text{MS}}$ renormalization constants $Z(\mu)$ can be written as

$$Z(\mu) = 1 + Z^{(1)}\frac{\alpha(\mu)}{4\pi} + Z^{(2)}\left(\frac{\alpha(\mu)}{4\pi}\right)^2 + \mathcal{O}\left(\frac{\alpha(\mu)}{4\pi}\right)^3, \quad (\text{B.1})$$

where each perturbative order $Z^{(n)}$ is expanded in powers of ϵ

$$Z^{(n)} = \sum_{m=0}^n Z^{(n,m)}\frac{1}{\epsilon^m}. \quad (\text{B.2})$$

The wavefunction renormalization constants, given by

$$\begin{aligned} Z_q^{(1)} &= -\frac{C_F}{\epsilon}\xi, \\ Z_q^{(2,2)} &= \frac{C_F}{4N_c}\xi(-\xi + 3N_c^2 + 2\xi N_c^2), \\ Z_q^{(2,1)} &= \frac{C_F}{8N_c}(-3 - 2\xi^2 - 22N_c^2 - 8\xi N_c^2 + \xi^2 N_c^2 + 4N_c f) - \frac{C_F^2}{2}\xi^2, \end{aligned} \quad (\text{B.3})$$

where $C_F = (N_c^2 - 1)/(2N_c)$ is the quadratic Casimir invariant for the defining representation of $SU(N_c)$ [37]. The gauge renormalization constant is defined as

$$Z_g^{(1)} = -\frac{\beta_0}{\epsilon}, \quad (\text{B.4})$$

where $\beta_0 = \frac{11}{3}N_c - \frac{2}{3}f$ [38], and the gauge parameter Z -factor is given by

$$Z_\xi^{(1)} = \left(N_c\left(\frac{5}{3} + \frac{1}{2}(1 - \xi)\right) - \frac{2}{3}f\right)\frac{1}{\epsilon}. \quad (\text{B.5})$$

C Operator anomalous dimensions

In order to perform the conversion between the two schemes at two-loop order, we will need two-loop $\overline{\text{MS}}$ renormalization constants. These can usually be extracted from the computation of the amplitude (or at least its poles). Alternatively, they enter the computation of the two-loop anomalous dimensions. Several such computations have been performed specifically for operator Q and can be found in [6, 7]. In this section we provide the derivation of the anomalous dimensions in our conventions.

In general, renormalized operators Q_i^{ren} can be expressed in terms of bare operators Q_i^{bare} , which have a well-defined meaning during the calculation, as defined in Eq.(2.11). The renormalization group equations of the operators

$$\mu \frac{d}{d\mu} Q_i^{\text{ren}}(\mu) = \gamma_{ij} Q_j^{\text{ren}}(\mu), \quad (\text{C.1})$$

are determined by the anomalous dimension matrix (ADM) γ_{ij} , defined via

$$\gamma_{ij} = \mu \frac{dZ_{ik}}{d\mu} Z_{kj}^{-1}. \quad (\text{C.2})$$

Hence, the one-loop ADM is given by

$$\gamma^{(0)} = -2Z^{(1,1)}. \quad (\text{C.3})$$

The coefficient in front of the $1/\epsilon$ pole has to vanish as the ADM has to be finite since it encodes the change of operators with the renormalization scale. Hence, one can obtain an ADM finiteness (or renormalisability) condition as

$$-2\beta_0 Z^{(1,1)} - 4Z^{(2,2)} + 2Z^{(1,1)} Z^{(1,1)} = 0. \quad (\text{C.4})$$

Finally, the two-loop ADM is given by

$$\gamma^{(1)} = (-2\beta_0 Z^{(1,0)} - 4Z^{(2,1)} + 2Z^{(1,0)} Z^{(1,1)} + 2Z^{(1,1)} Z^{(1,0)}). \quad (\text{C.5})$$

As long as $\gamma^{(0)}$ arises at one-loop, as is the case in our investigation, it is scheme-independent. The $\gamma^{(1)}$ generally depend on the renormalization scheme as $Z^{(1,0)}$ and $Z^{(2,1)}$ usually depend on the choice of the evanescent operators, conventionally chosen such that their Green's functions vanish in four dimensions.

D One-loop counterterms

Adding all 6 diagrams, for the one-loop amplitude we obtain

$$\begin{aligned} \langle Q \rangle^{1\text{-loop}} &= \frac{\alpha_s}{4\pi} \frac{1}{\epsilon} \left\{ \left(2C_F \xi - 3 \left(1 - \frac{1}{N_c} \right) \right) \langle Q \rangle - 3 \langle E_F \rangle + \frac{1}{2N_c} \langle E_1 \rangle - \frac{1}{2} \langle E_2 \rangle \right\} \\ &+ \mathcal{O}(\epsilon^0). \end{aligned} \quad (\text{D.1})$$

From the requirement $Z_q^2 \langle Q^{\overline{\text{MS}}} \rangle = \text{finite}$, where $Z_q = 1 - C_F \xi \alpha_s / (4\pi\epsilon)$ is the 1-loop $\overline{\text{MS}}$ field renormalization constant in a general covariant gauge [17], the $\alpha_s/(4\pi)$ coefficients in the Z -factors can then be read-off as

$$Z_{QQ}^{(1)} = \frac{3}{\epsilon} \left(1 - \frac{1}{N_c} \right), \quad Z_{QE_2}^{(1)} = \frac{1}{2\epsilon}, \quad (\text{D.2})$$

$$Z_{QE_F}^{(1)} = \frac{3}{\epsilon}, \quad Z_{QE_3}^{(1)} = 0, \quad (\text{D.3})$$

$$Z_{QE_1}^{(1)} = -\frac{1}{2N_c\epsilon}, \quad Z_{QE_4}^{(1)} = 0. \quad (\text{D.4})$$

In addition, for the two-loop renormalization we also require additional one-loop Z factors corresponding to the evanescent operators E_F , E_1 and E_2 . We obtain them via insertions of the evanescent operators into the vertices of the one-loop diagrams. Inserting E_F into the vertex yields

$$\begin{aligned} \langle E_F \rangle^{1\text{-loop}} = & \frac{\alpha_s}{4\pi} \frac{1}{\epsilon} \left\{ \left(2C_F \xi + 3 \left(1 + \frac{1}{N_c} \right) \right) \langle E_F \rangle \right. \\ & \left. - \left(\frac{1}{4} + \frac{1}{2N_c} \right) \langle E_1 \rangle + \left(\frac{1-C_F}{2} + \frac{1}{4N_c} \right) \langle E_2 \rangle \right\} + \mathcal{O}(\epsilon^0), \end{aligned} \quad (\text{D.5})$$

giving the constants

$$Z_{E_F Q}^{(1)} = 0, \quad Z_{E_F E_2}^{(1)} = \frac{1}{\epsilon} \left(\frac{C_F - 1}{2} - \frac{1}{4N_c} \right), \quad (\text{D.6})$$

$$Z_{E_F E_F}^{(1)} = -\frac{3}{\epsilon} \left(1 + \frac{1}{N_c} \right), \quad Z_{E_F E_3}^{(1)} = 0, \quad (\text{D.7})$$

$$Z_{E_F E_1}^{(1)} = \frac{1}{\epsilon} \left(\frac{1}{4} + \frac{1}{2N_c} \right), \quad Z_{E_F E_4}^{(1)} = 0. \quad (\text{D.8})$$

Similarly, the remaining Z factors have been obtained from the corresponding insertions into the one-loop amplitudes

$$\begin{aligned} \langle E_1 \rangle^{1\text{-loop}} = & \frac{\alpha_s}{4\pi} \frac{1}{\epsilon} \left\{ \left(2C_F \xi - \frac{13}{N_c} \right) \langle E_1 \rangle + 13 \langle E_2 \rangle + \frac{1}{2N_c} \langle E_3 \rangle - \frac{1}{2} \langle E_4 \rangle \right\} \\ & + 24 \left(2C_F + 1 - \frac{1}{N_c} \right) \langle Q \rangle + \text{evanescent}, \end{aligned} \quad (\text{D.9})$$

$$\begin{aligned} \langle E_2 \rangle^{1\text{-loop}} = & \frac{\alpha_s}{4\pi} \frac{1}{\epsilon} \left\{ 5 \langle E_1 \rangle + \left(2C_F \xi + 16C_F - \frac{5}{N_c} \right) \langle E_2 \rangle - \frac{1}{4} \langle E_3 \rangle \right. \\ & \left. + \frac{1}{4} \left(\frac{1}{N_c} - 2C_F \right) \langle E_4 \rangle \right\} + 48 \left(1 - \frac{1}{N_c} \right) \langle Q \rangle + \text{evanescent}, \end{aligned} \quad (\text{D.10})$$

where ‘‘evanescent’’ denotes terms that vanish as $D \rightarrow 4$. The renormalization constants can then be read-off as

$$Z_{E_1 E_F}^{(1)} = 0, \quad Z_{E_2 E_F}^{(1)} = 0, \quad (\text{D.11})$$

$$Z_{E_1 E_1}^{(1)} = \frac{13}{N_c \epsilon}, \quad Z_{E_2 E_1}^{(1)} = -\frac{5}{\epsilon}, \quad (\text{D.12})$$

$$Z_{E_1 E_2}^{(1)} = -\frac{13}{\epsilon}, \quad Z_{E_2 E_2}^{(1)} = \frac{1}{\epsilon} \left(\frac{5}{N_c} - 16 C_F \right), \quad (\text{D.13})$$

$$Z_{E_1 E_3}^{(1)} = -\frac{1}{2N_c \epsilon}, \quad Z_{E_2 E_3}^{(1)} = \frac{1}{4\epsilon}, \quad (\text{D.14})$$

$$Z_{E_1 E_4}^{(1)} = \frac{1}{2\epsilon}, \quad Z_{E_2 E_4}^{(1)} = \frac{1}{4\epsilon} \left(2 C_F - \frac{1}{N_c} \right). \quad (\text{D.15})$$

The properly renormalized evanescent operators also require a subtraction of the finite constants multiplying $\langle Q \rangle$, giving

$$Z_{E_1 Q}^{(1)} = 24 \left(2 C_F + 1 - \frac{1}{N_c} \right), \quad Z_{E_2 Q}^{(1)} = 48 \left(1 - \frac{1}{N_c} \right). \quad (\text{D.16})$$

E Two-loop counterterms

Two-loop Z factors can be extracted from the 2-loop ADM. The Z factor can be expanded as

$$Z^{(2)} = \left(\frac{1}{\epsilon} Z^{(2,1)} + \frac{1}{\epsilon^2} Z^{(2,2)} \right), \quad (\text{E.1})$$

Recalling the ADM finiteness limit in Eq.(C.4), given by

$$4Z^{(2,2)} + 2\beta_0 Z^{(1,1)} - 2Z^{(1,1)} Z^{(1,1)} = 0, \quad (\text{E.2})$$

where $\beta_0 = (11N_c - 2f)/3$, we get

$$Z_{QQ}^{(2,2)} = \frac{1}{2} (Z_{QQ}^{(1,1)})^2 - \frac{1}{2} Z_{QQ}^{(1,1)} \beta_0 = -\frac{(N_c - 1)(N_c(-2f + 11N_c - 9) + 9)}{2N_c^2}, \quad (\text{E.3})$$

$$Z_{QE_F}^{(2,2)} = \frac{1}{2} (Z_{QQ}^{(1,1)} Z_{QE_F}^{(1,1)} + Z_{E_F E_F}^{(1,1)} Z_{QE_F}^{(1,1)}) - \frac{1}{2} Z_{QE_F}^{(1,1)} \beta_0 = f - \frac{11N_c}{2} - \frac{9}{N_c}. \quad (\text{E.4})$$

Using Eq.(5.2) of [6], which translated to our conventions is written as

$$\gamma_{QQ}^{(1)} = \frac{(N_c - 1)}{2N_c} \left(21 - \frac{57}{N_c} + \frac{19}{3} N_c - \frac{4}{3} f \right), \quad (\text{E.5})$$

and Eq.(C.5), given by

$$\gamma_{QQ}^{(1)} = -4Z_{QQ}^{(2,1)} + 2Z_{QE_1}^{(1,1)} Z_{E_1 Q}^{(1,0)}, \quad (\text{E.6})$$

we get

$$Z_{QQ}^{(2,1)} = \frac{N_c(-288C_F + N_c(19N_c - 4f + 44) + 4f - 378) + 315}{24N_c^2}. \quad (\text{E.7})$$

Technically, $Z_{QE_F}^{(2,1)}$ also enters the two-loop amplitude, however, we find that it drops out of the computation of A' , hence it is not essential.

Finally, the change of basis between our and BG evanescent operator basis can be obtained in terms of $1/\epsilon^2$ parts of renormalization constants. To convert to the BG scheme, we require two two-loop $1/\epsilon^2$ pole coefficients in the evanescent sector. They can be inferred from the Eq.(C.4) as

$$Z_{QE_3}^{(2,2)} = Z_{QE_1}^{(1)} Z_{E_1 E_3}^{(1)} + Z_{QE_2}^{(1)} Z_{E_2 E_3}^{(1)} = \frac{1}{4N_c^2} + \frac{1}{8}, \quad (\text{E.8})$$

$$Z_{QE_4}^{(2,2)} = Z_{QE_1}^{(1)} Z_{E_1 E_4}^{(1)} + Z_{QE_2}^{(1)} Z_{E_2 E_4}^{(1)} = \frac{C_F}{4} - \frac{3}{8N_c}. \quad (\text{E.9})$$

References

- [1] A. J. Buras, M. Jamin and P. H. Weisz, *Leading and Next-to-leading QCD Corrections to ϵ Parameter and $B^0 - \bar{B}^0$ Mixing in the Presence of a Heavy Top Quark*, *Nucl. Phys. B* **347** (1990) 491.
- [2] J. Brod, M. Gorbahn and E. Stamou, *Standard-Model Prediction of ϵ_K with Manifest Quark-Mixing Unitarity*, *Phys. Rev. Lett.* **125** (2020) 171803 [[1911.06822](#)].
- [3] A. J. Buras and D. Guadagnoli, *Correlations among new CP violating effects in $\Delta F = 2$ observables*, *Phys. Rev. D* **78** (2008) 033005 [[0805.3887](#)].
- [4] A. J. Buras, D. Guadagnoli and G. Isidori, *On ϵ_K Beyond Lowest Order in the Operator Product Expansion*, *Phys. Lett. B* **688** (2010) 309 [[1002.3612](#)].
- [5] G. Buchalla, A. J. Buras and M. E. Lautenbacher, *Weak decays beyond leading logarithms*, *Rev. Mod. Phys.* **68** (1996) 1125 [[hep-ph/9512380](#)].
- [6] A. J. Buras and P. H. Weisz, *QCD Nonleading Corrections to Weak Decays in Dimensional Regularization and 't Hooft-Veltman Schemes*, *Nucl. Phys. B* **333** (1990) 66.
- [7] J. Brod and M. Gorbahn, *ϵ_K at Next-to-Next-to-Leading Order: The Charm-Top-Quark Contribution*, *Phys. Rev.* **D82** (2010) 094026 [[1007.0684](#)].
- [8] J. Brod and M. Gorbahn, *Next-to-Next-to-Leading-Order Charm-Quark Contribution to the CP Violation Parameter ϵ_K and ΔM_K* , *Phys. Rev. Lett.* **108** (2012) 121801 [[1108.2036](#)].
- [9] J. Brod, S. Kvedaraitė and Z. Polonsky, *Two-loop electroweak corrections to the Top-Quark Contribution to ϵ_K* , *JHEP* **12** (2021) 198 [[2108.00017](#)].
- [10] J. Brod, S. Kvedaraitė, Z. Polonsky and A. Youssef, *Electroweak corrections to the Charm-Top-Quark Contribution to ϵ_K* , *JHEP* **12** (2022) 014 [[2207.07669](#)].
- [11] M. Ciuchini, E. Franco, V. Lubicz, G. Martinelli, L. Silvestrini and C. Tarantino, *Power corrections to the CP-violation parameter ϵ_K* , *JHEP* **02** (2022) 181 [[2111.05153](#)].
- [12] PARTICLE DATA GROUP collaboration, *Review of Particle Physics*, *PTEP* **2022** (2022) 083C01.
- [13] FLAVOUR LATTICE AVERAGING GROUP (FLAG) collaboration, *FLAG Review 2024*, [2411.04268](#).
- [14] RBC AND UKQCD COLLABORATIONS collaboration, *Renormalization of quark bilinear operators in a momentum-subtraction scheme with a nonexceptional subtraction point*, *Phys. Rev. D* **80** (2009) 014501.

- [15] G. Martinelli, C. Pittori, C. T. Sachrajda, M. Testa and A. Vladikas, *A General method for nonperturbative renormalization of lattice operators*, *Nucl. Phys. B* **445** (1995) 81 [[hep-lat/9411010](#)].
- [16] A. J. Buras, *Weak Hamiltonian, CP violation and rare decays*, in *Les Houches Summer School in Theoretical Physics, Session 68: Probing the Standard Model of Particle Interactions*, pp. 281–539, 6, 1998, [hep-ph/9806471](#).
- [17] Y. Aoki et al., *Continuum Limit of B_K from 2+1 Flavor Domain Wall QCD*, *Phys. Rev. D* **84** (2011) 014503 [[1012.4178](#)].
- [18] K. Chetyrkin and F. Tkachov, *Integration by Parts: The Algorithm to Calculate beta Functions in 4 Loops*, *Nucl. Phys. B* **192** (1981) 159.
- [19] S. Kvedaraitė, *From Flavour and Higgs Precision Physics to LHC Discoveries*, Ph.D. thesis, Sussex U., 2021.
- [20] A. von Manteuffel and C. Studerus, *Reduze 2 - Distributed Feynman Integral Reduction*, [1201.4330](#).
- [21] S. Laporta, *High precision calculation of multiloop Feynman integrals by difference equations*, *Int. J. Mod. Phys. A* **15** (2000) 5087 [[hep-ph/0102033](#)].
- [22] N. I. Usyukina and A. I. Davydychev, *New results for two loop off-shell three point diagrams*, *Phys. Lett. B* **332** (1994) 159 [[hep-ph/9402223](#)].
- [23] T. Gehrmann and E. Remiddi, *Differential equations for two loop four point functions*, *Nucl. Phys. B* **580** (2000) 485 [[hep-ph/9912329](#)].
- [24] S. Borowka, G. Heinrich, S. Jahn, S. Jones, M. Kerner, J. Schlenk et al., *pySecDec: a toolbox for the numerical evaluation of multi-scale integrals*, *Comput. Phys. Commun.* **222** (2018) 313 [[1703.09692](#)].
- [25] J. Gracey, *Three loop anomalous dimension of nonsinglet quark currents in the RI-prime scheme*, *Nucl. Phys. B* **662** (2003) 247 [[hep-ph/0304113](#)].
- [26] M. Gorbahn and S. Jager, *Precise \overline{MS} light-quark masses from lattice QCD in the RI/SMOM scheme*, *Phys. Rev. D* **82** (2010) 114001 [[1004.3997](#)].
- [27] PARTICLE DATA GROUP collaboration, *Review of particle physics*, *Phys. Rev. D* **110** (2024) 030001.
- [28] K. Chetyrkin, J. H. Kuhn and M. Steinhauser, *RunDec: A Mathematica package for running and decoupling of the strong coupling and quark masses*, *Comput. Phys. Commun.* **133** (2000) 43 [[hep-ph/0004189](#)].
- [29] RBC, UKQCD collaboration, *Kaon mixing beyond the standard model with physical masses*, *Phys. Rev. D* **110** (2024) 034501 [[2404.02297](#)].
- [30] RBC/UKQCD collaboration, *Neutral Kaon Mixing Beyond the Standard Model with $n_f = 2 + 1$ Chiral Fermions Part 1: Bare Matrix Elements and Physical Results*, *JHEP* **11** (2016) 001 [[1609.03334](#)].
- [31] BMW collaboration, *Precision computation of the kaon bag parameter*, *Phys. Lett. B* **705** (2011) 477 [[1106.3230](#)].
- [32] ETM collaboration, *$\Delta S=2$ and $\Delta C=2$ bag parameters in the standard model and beyond from $N_f=2+1+1$ twisted-mass lattice QCD*, *Phys. Rev. D* **92** (2015) 034516 [[1505.06639](#)].

- [33] SWME collaboration, *Kaon BSM B-parameters using improved staggered fermions from $N_f = 2 + 1$ unquenched QCD*, *Phys. Rev. D* **93** (2016) 014511 [[1509.00592](#)].
- [34] RBC, UKQCD collaboration, *Domain wall QCD with physical quark masses*, *Phys. Rev. D* **93** (2016) 074505 [[1411.7017](#)].
- [35] J. Laiho and R. S. Van de Water, *Pseudoscalar decay constants, light-quark masses, and B_K from mixed-action lattice QCD*, *PoS LATTICE2011* (2011) 293 [[1112.4861](#)].
- [36] M. Schmelling, *Averaging correlated data*, *Phys. Scripta* **51** (1995) 676.
- [37] E. Franco and V. Lubicz, *Quark mass renormalization in the \overline{ms} and \overline{ri} schemes up to the $nnlo$ order*, *Nuclear Physics B* **531** (1998) 641.
- [38] L. N. Mihaila, J. Salomon and M. Steinhauser, *Renormalization constants and beta functions for the gauge couplings of the standard model to three-loop order*, *Phys. Rev. D* **86** (2012) 096008.